The Dissertation Committee for Daniel Glen Sheppard
certifies that this is the approved version of the following dissertation:

Methods for Calculating Chemical Properties in the Condensed Phase

Committee:

Graeme A. Henkelman, Supervisor

C. Buddie Mullins

Peter J. Rossky

David A. Vanden Bout

Gyeong S. Hwang

Methods for Calculating Chemical Properties in the Condensed Phase

by

Daniel Glen Sheppard, B.S.

DISSERTATION

Presented to the Faculty of the Graduate School of
The University of Texas at Austin
in Partial Fulfillment
of the Requirements
for the Degree of

DOCTOR OF PHILOSOPHY

THE UNIVERSITY OF TEXAS AT AUSTIN
December 2010

Dedicated to my wife Julia and all my children.

Acknowledgments

I wish to give a special thanks to my advisor Graeme Henkelman who not only put up with my graduate school antics but also pushed me to strive for excellence. His pragmatic approach to problem solving and straight forward communication skills made him a pleasure to work with. I would also like to thank all my co-authors and collaborators who helped me overcome the research and writing process. Lastly I would like to thank my loving wife who, for some reason, not only tolerates me but also helps remind me what is truly important.

Methods for Calculating Chemical Properties in the Condensed Phase

Publication No. ____________________

Daniel Glen Sheppard, Ph.D.
The University of Texas at Austin, 2010

Supervisor: Graeme A. Henkelman

With advancements in computer technology and processing power, the ability to examine chemical systems using theory continues to be more practicable. Using *ab initio* methods, such as density functional theory, we are now able to routinely simulate hundreds of atoms. This system size allows us to directly simulate surfaces and nano-materials that are industrially relevant. With the expansion of accessible systems comes the opportunity to develop new computational methods to extract their chemical properties.

Of particular interest is bridging the time scale gap between simulation and experiment. The evolution of a system chemical in time can be directly simulated using classical dynamics, however, molecules vibrate on the order of *femto*seconds and interesting transitions tend to happen on much longer time scales: *milli*seconds to seconds. In condensed phase chemical systems these interesting transitions are hindered by energy barriers so state to state dynamics are dominated by rare evens. Luckily, rare event transitions tend to happen through mountain passes in the potential energy landscape. Within harmonic transition state theory, the transition states between minima can be characterized by saddle points. Finding saddle points is a challenging problem which has not been satisfactorily solved; nevertheless, there are algorithms currently being used despite their deficiency. In particular, my work strives to improve the efficiency and stability of the nudged elastic band method and compare its performance to similar algorithms on a variety of test systems.

In addition, I present a method to predict how energy-based chemical properties change with respect to the chemical composition of the system. This is achieved by taking a derivative of the property with respect to the atomic numbers of the atoms present in the system. The accuracy and predictive quality of these derivatives are assessed for both model and industrially relevant systems. With this information, we can follow these derivatives to optimize a desired property in the space of chemical composition. This method is a step toward using theory to rationally design compounds with desirable properties.

Table of Contents

List of Figures

List of Tables

Glossary

AB INITIO: (first principles) Solving the electron structure from Schrödinger's equation without using fit empirical data. DFT is often considered an *ab initio* method even though the electron exchange-correlation functionals are typically tuned using experimental data.

ALCHEMICAL DERIVATIVE: The derivative of the potential energy of a compound with respect to its chemical identity.

ALCHEMICAL POTENTIAL: Analogous to the chemical potential, the energy gained or lost by inserting or removing a proton.

CG: Conjugate gradients.

CI-NEB: Climbing image nudged elastic band.

CLIMBING IMAGE NUDGED ELASTIC BAND: A variation of the NEB where the highest energy image climbs, finding the maximum along the path, which is the saddle point.

CONJUGATE GRADIENTS: A force based optimization method which uses the previous direction moved and the current force to chose a "better" direction for the next optimization step.

DENSITY FUNCTIONAL THEORY: A method to solve the quantum mechanical electronic structure of a system of electrons using the electron density. This method is typically used with large systems due to its low cost, compared to wave-function based methods.

DFT: Density functional theory.

DNEB: Doubly nudged elastic band.

DOUBLY NUDGED ELASTIC BAND: A variation on the NEB where part of the perpendicular spring force is kept to speed up optimization of the MEP.

FAST INERTIAL RELAXATION ENGINE: An optimization method based on dynamics with a variable time step and where most of the velocity not in the force direction is damped.

FIRE: Fast Inertial Relaxation Engine.

GE: Gradient Extremal.

GRADIENT EXTREMAL: A set of points where the gradient is an eigenvector of the Hessian matrix.

HARMONIC TRANSITION STATE THEORY: An approximation to TST where the transition state reduces to a saddle point.

HESSIAN MATRIX: A 3N × 3N matrix where the components are second derivatives of the energy with respect to position.

HOMO: Highest occupied molecular orbital.

HTST: Harmonic transition state theory.

L-BFGS: Limited-memory Broyden-Fletcher-Goldfarb-Shanno.

LIMITED-MEMORY BROYDEN-FLETCHER-GOLDFARB-SHANNO: A second order optimization method where an approximate Hessian matrix is updated using gradients and positions of the last m steps.

LUMO: Lowest unoccupied molecular orbital.

MEP: Minimum energy path.

MINIMUM ENERGY PATH: A set of points connecting two minima on a PES which are minima in the hyperplane perpendicular to the path.

NEB: Nudged elastic band.

NUDGED ELASTIC BAND: A method for finding the saddle point and subsequent SD path between two adjacent minima on a PES where forces perpendicular to the path are minimized and the images are evenly spaced by tangental acting spring forces.

ORR: Oxygen reduction reaction.

PES: Potential energy surface.

POTENTIAL ENERGY SURFACE: A typically multidimensional hyper-surface, constructed within the Born-Oppenheimer approximation, which maps the energy to position of the atoms.

QM: Quick-min

QUICK-MIN: An optimization method based on dynamics where only the velocity along the force direction is perserved.

SADDLE POINT: A point on the PES where all forces are zero and the Hessian matrix has one negative curvature mode. This visually looks like a mountain pass.

SD: Steepest descent.

SIMPLIFIED STRING METHOD: A variation of the string method which does not use force projections.

SP: Saddle point.

STEEPEST DESCENT: A set of points following the negative gradient from the maximum along the path to a minimum.

STM: Scanning tunneling microscopy.

STRING METHOD: A method for finding saddle points analogous to the NEB where instead of using springs the images are redistributed along a spline to maintain equal spacing along the path.

TRANSITION STATE: A hyper-surface containing a bottleneck for a reaction between tow stable states on a PES; transition state is characterized by a saddle point within HTST.

TRANSITION STATE THEORY: A theory used to calculate reaction rates as an equilibrium flux through a transition state.

TST: Transition state theory.

UHV: Ultra high vacuum.

ULTRA HIGH VACUUM: A vacuum regime characterized by pressures less than 10^{-9} torr. Experiments performed in UHV can be directly compared to simulations in vacuum.

Chapter 1

Introduction

This dissertation is comprised of my work as a graduate student in physical chemistry at the University of Texas at Austin. This work revolves around improving current computational methods and designing new methods used for studying chemical properties in the condensed phase. Each chapter presented is a previously published paper written with Graeme Henkelman and our collaborators and directly addresses or uses the methods to study an interesting application. Rye Terrell championed the string method work from Chapter 2. Chapter 4 is the theoretical part of a combined study with Shao-Chun Li, Zhenrong Zhang, Bruce Kay, Yingge Du, Igor Lyubinetsky, and Zdenek Dohnalek. Anatole von Lilienfeld was the main motivator behind the alchemy project, Chapter 5. In this introduction, I will briefly motivate the work behind each chapter.

1.1 Optimization Methods for Finding Minimum Energy Paths

A minimum energy path is a continuous path that connects two states in which the potential energy is a minium perpendicular to the path. The perpendicular hyper-surface defined at a maximum on the minimum energy path between two adjacent minima is the saddle point. Once the transition state is characterized, transition state theory is used to extract information about reaction kinetics from the reaction energetics. Solid systems have well-defined modes of vibration and transitions can be described by harmonic basins at minima and saddle points. Within harmonic transition state theory (HTST), finding a transition state reduces to finding a saddle point (one negative mode) on a high dimensional–3 times N atoms–potential energy surface [1]. The HTST rate, k, for a transition follows the Arrhenius form:

$$k = \nu^{\dagger} e^{-\Delta E / K_{\mathrm{B}} T} \tag{1.1}$$

where $\Delta E = E^{\mathrm{ts}} - E^{\mathrm{min}}$ is the difference in energy between the saddle point (E^{ts}) and energy at the minimum (E^{min}). The harmonic prefactor, $\nu^{\dagger}$ is

$$\nu^{\dagger} = \frac{\prod^{N_\nu} \nu_i^{\mathrm{min}}}{\prod^{N_\nu - 1} \nu_i^{\mathrm{ts}}} \tag{1.2}$$

where ν_i^{min} and ν_i^{ts} are the normal modes for the minimum and transition state configurations respectively and N_ν is the number of non-zero vibrational modes in the system. The negative mode at the transition state is not included in the calculation of $\nu^{\dagger}$.

Although exact reaction rates can be calculated using molecular dynamics (MD), the time scales accessible (∼ns) are typically much shorter than the time scales for reactions of interest (μs-s). Combining the time scale disparity with the expense of using first principles to evaluate potential energies and atomic forces and simulations becomes unwieldy, making HTST a pragmatic solution for chemical kinetics in condensed phase systems. Despite the speedup from HTST over MD, the cost of using a high number of atoms required to model surface chemistry by first principles is not trivial. It is imperative that saddle point finding algorithms work efficiently. In an effort to model the kinetics of surface reactions more timely, the effect of optimizer choice and implementation is studied for two-ended saddle point search methods: the nudged elastic band method, the double-nudged elastic band method, the string method, and the new string method. In addition, well-defined benchmark systems and convergence criteria are introduced to facilitate future algorithmic comparisons.

1.2 Paths to which the nudged elastic band converges

In this brief letter to the editor, we clarify that the NEB formally converges to the steepest decent (SD) path from the saddle. While the SD path is typically also an MEP for elementary transitions, sometimes the MEP terminates at an inflection point. When this happens, the NEB will continue to follow the SD path and not the MEP. This is shown to happen for adatom diffusion on the Al(110) surface.

1.3 Intrinsic Diffusion of Hydrogen on Rutile TiO_2(110)

Using an efficient algorithm for finding transition states allows us to study and obtain kinetic data on large systems with direct application to experiments. Here we use an optimized nudged elastic band method to study the diffusion of oxygen vacancies and the hydrogen from adsorbed H_2O on a rutile $TiO_2(110)$ surface. This process has direct application for understanding the use ofTiO_2 for water-splitting and hydrogen gas production. The purpose of this experimental and theoretical study is to better understand the mechanistic and physical properties of TiO_2 on the molecular level. In the case of hydrogen diffusion, classical HTST alone did not match experimental energy barriers and prefactors, so we also included quantum zero-point corrections and tunneling corrections to the calculated rates.

1.4 Alchemical Derivatives of Reaction Energetics

In the next chapter we work on the reverse problem, tuning chemical systems to have desired reaction energetics. I propose to advance theory's ability to guide experimentalists in the design of compounds by presenting a method for using alchemical derivatives of reaction energetics to aid in the tuning of compounds for desired properties. For example, when designing a catalyst their is a trade off between activating the reactants and the reactants binding energy to the catalyst[2]. Alchemical derivatives can predict how to change the catalyst to optimize the balance of these properties. An analytical expression for the derivative of the energy functional with respect to number of protons in the nuclei is presented within grand-canonical density functional theory (DFT). This expression gives the first order energy response to changing the identity of the nuclei in the system. Because the number of protons is used to identify the element for each atom, this derivative with respect to number of protons is called an “alchemical” derivative. The alchemical derivative is taken from the electrostatic potential which we get at no additional cost while calculating the potential energy and force from DFT. An alchemical derivative is then straight forward to define for any property derived from the potential energy such as the following: binding energies, activation energies, heat of formations, HOMO and LUMO eigenvalues, and band-gaps. We can then minimize along these alchemical derivatives the same way we would use the force to optimize a configuration. In this way, we move through the configurational space made up of all atoms in a rational way. Using these derivatives, we highlight the parts of space that move toward the target property while ignoring the irrelevant parts of chemical space.

In this chapter we assess the accuracy of the analytical alchemical derivatives compared with finite difference alchemical derivatives to validate the derivation. We then examine how predictive the derivatives are for integer changes to the number of protons on a 79 atom Pd nano-particle with the intent to show their potential usefulness for catalyst design.

Improving current computational methods is a vital step toward evolving theoretical chemistry into a predictive tool that can be used to guide experimentalist rather than a successive science which only confirms and elucidates experimental work.

Chapter 2

Optimization Methods for Finding Minimum Energy Paths

2.1 Abstract

A comparison of chain-of-states based methods for finding minimum energy pathways (MEPs) is presented. In each method, a set of images along an initial pathway between two local minima is relaxed to find a MEP. We compare the nudged elastic band (NEB), doubly nudged elastic band, string, and simplified string methods, each with a set of commonly-used optimizers. Our results show that the NEB and string methods are essentially equivalent and the most efficient methods for finding MEPs when coupled with a suitable optimizer. The most efficient optimizer was found to be a form of the limited-memory Broyden-Fletcher-Goldfarb-Shanno (L-BFGS) method in which the approximate inverse Hessian is constructed globally for all images along the path. Use of a climbing-image allows for finding the saddle point while representing the MEP with as few images as possible. If a highly accurate MEP is desired, it is found to be more efficient to descend from the saddle to the minima than to use a chain-of-states method with many images. Our results are based upon a pairwise Morse potential to model rearrangements of a heptamer island on Pt(111), and plane wave based density functional theory to model a

roll-over diffusion mechanism of a Pd tetramer on MgO(100) and dissociative adsorption and diffusion of oxygen on Au(111).

2.2 Introduction

Computational methods for calculating minimum energy paths (MEPs) are widely used in the fields of theoretical chemistry, physics, and materials science. The MEP describes the mechanism of reaction, and in thermal systems, the energy barrier along the path can be used to calculate the reaction rate.

Here, we compare several approaches for finding MEPs. We have restricted our investigation to methods in which the initial and final states are known. Our goal is then to find the MEP between these states to a specified accuracy with the smallest amount of computational effort.

This paper is structured in the following way. In Sec. 2.3, the nudged elastic band (NEB) method [3, 4, 5], is summarized. In Sec. 2.4 we state our objectives and convergence criteria for finding MEPs. In Sec. 2.5 we describe the optimizers that we use to converge the NEB. Convergence results are presented in Sec. 2.6 for a model system of island rearrangement on a (111) surface using a pairwise Morse potential.

Using the NEB as a baseline, recently developed methods are compared in subsequent sections. These include the doubly nudged elastic band (DNEB) [6] (Sec. 2.7), the string [7] (Sec. 2.8), and the simplified string [8] (Sec. 2.9) methods.

Finally, we reproduce our NEB optimizer tests for three different surface reactions modeled with density functional theory: in Sec. 2.10.1, Pd_4 diffusion on MgO(100), and in Sec. 2.10.2, O_2 dissociative adsorption and O diffusion on Au(111).

2.3 Nudged Elastic Band Method

The NEB is a method to find a MEP between a pair of stable states [3]. In the context of reaction rates, this pair has an initial and a final state, both of which are local minima on the potential energy surface (PES). The MEP has the property that any point on the path is at an energy minimum in all directions perpendicular to the path. This path passes through at least one first-order saddle point. The MEP can also be described as the union of steepest decent paths from the saddle point(s) to the minima.

The NEB is a chain-of-states method [9, 10] in which a string of images (geometric configurations of the system) are used to describe a reaction pathway. These configurations are connected by spring forces to ensure equal spacing along the reaction path. Upon convergence of the NEB to the MEP, the images describe the reaction mechanism, up to the resolution of the images (see Fig. 2.1).

A NEB calculation is started from an initial pathway connecting initial and final states. Typically, a linear initial path is sufficient, but in some cases,

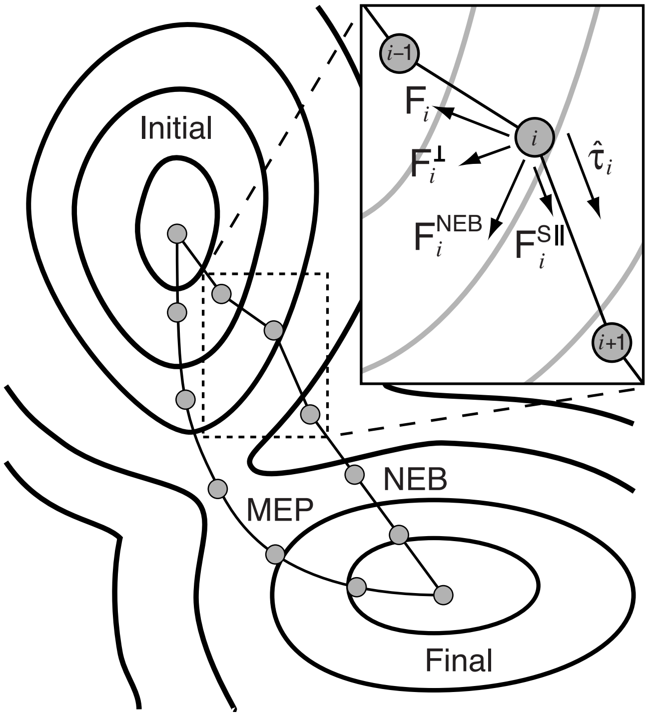

Figure 2.1: Two components make up the nudged elastic band force, $\mathbf{F}^{\mathrm{NEB}}$: the spring force, $\mathbf{F}_i^{\mathrm{S}\parallel}$, along the tangent, $\hat{\boldsymbol{\tau}}_i$, and the perpendicular force due to the potential, $\mathbf{F}_i^{\perp}$. The unprojected force do to the potential, $\mathbf{F}_i$, is also shown for completeness.

a different choice is better. For example, if atoms get close to each other along the linear path, a geometric repulsive force can be used to push these atoms apart, resulting in a band with lower initial forces. An interpolation in internal coordinates can also yield a more suitable initial pathway [11], for example, if the reaction involves rotational motion. When the reaction is known to go through an intermediate state, an initial path can be constructed from segments through the intermediate.

The images along the NEB are relaxed to the MEP through a force projection scheme in which potential forces act perpendicular to the band, and spring forces act along the band. To make these projections, the tangent along the path, $\hat{\boldsymbol{\tau}}$, is defined as the unit vector to the higher energy neighboring image [4]. A linear interpolation between the vectors to neighboring images is used at extrema so that the definition of $\hat{\boldsymbol{\tau}}$ does not change abruptly. This upwinding tangent improves the stability of the NEB and avoids the development of artificial kinks in high force regions along the path [4].

The NEB force on image i contains two independent components,

$$\mathbf{F}_i^{\mathrm{NEB}} = \mathbf{F}_i^{\perp} + \mathbf{F}_i^{\mathrm{S}\|}, \tag{2.1}$$

where $\mathbf{F}_i^{\perp}$ is the component of the force, due to the potential, perpendicular to the band,

$$\mathbf{F}_i^{\perp} = -\nabla(\mathbf{R}_i) + \nabla(\mathbf{R}_i) \cdot \hat{\boldsymbol{\tau}}_i \hat{\boldsymbol{\tau}}_i, \tag{2.2}$$

and $\mathbf{F}_i^{\mathrm{S}\|}$ is the spring force parallel to the band,

$$\mathbf{F}_i^{\mathrm{S}\|} = k \left(|\mathbf{R}_{i+1} - \mathbf{R}_i| - |\mathbf{R}_i - \mathbf{R}_{i-1}| \right) \hat{\boldsymbol{\tau}}_i. \tag{2.3}$$

In this final expression, $\mathbf{R}_i$ is the position of the i^{th} image and k is the spring constant.

The saddle point is particularly important for characterizing the transition state within harmonic transition state theory (TST). The difference between the saddle point energy and that of the initial state determines the exponential term in the Arrhenius rate, and the MEP can be obtained by minimizing from the saddle point(s). An efficient strategy for finding a saddle between known states is to roughly optimize a NEB calculation, and then do a min-mode following saddle-point search [12, 13] from the highest energy image to find the transition state [4, 6]. Another approach, which avoids having to run two separate optimizations or interpolate to find the saddle, is the climbing-image NEB (CI-NEB) [5]. In this method, the highest energy image, l, feels no spring forces and climbs to the saddle via a reflection in the force along the tangent,

$$\mathbf{F}_l^{\mathrm{CI}} = \mathbf{F}_l - 2\mathbf{F}_l \cdot \hat{\boldsymbol{\tau}}_l \hat{\boldsymbol{\tau}}_l. \tag{2.4}$$

Once the saddle is found, the normal mode frequencies can be calculated to ensure that the saddle is first order, and to find the prefactor of the reaction.

2.4 Convergence Objectives

The methods tested here are evaluated using the following optimization objectives and convergence criteria.

Our principle goal is to compare methods as they are used by researchers who do calculations of reaction pathways in chemistry and materials science. Most of these methods have parameters that can be tuned to optimize performance. Our approach is to determine a set of near-optimal parameters which can be used for all tests, rather than re-optimize the parameters for each calculation. This strategy reflects the way computational methods are normally used; there is little advantage to a method that requires significant additional calculations for parameter tuning.

Our objective is to find minimum energy pathways between stationary states. Specifically how this objective is defined, however, can lead to different conclusions about which methods are efficient. Thus, we need to clarify exactly what we are interested in calculating, and emphasize that our tests reflect the bias of chemistry and material science, in which MEPs are calculated to find both the mechanism and activation energy of reactions.

Generally, a researcher wants to understand the mechanism (the geometric pathway) of reaction qualitatively, and the activation energy with higher accuracy. By a qualitative reaction pathway, we mean that intermediate minima along the pathway should be identified by the MEP search. By an accurate activation energy, we mean that in principle, the saddle point energy could be found to arbitrary accuracy on a given potential energy surface, but in practice, it should be known well enough to give an accurate harmonic TST rate. In these tests, a climbing image approach is used so that one image along the band is converged to the saddle point to a specified precision [5].

In this study, we investigate single step reaction mechanisms where eight or fewer images can be used to resolve the MEP. The number of images was kept fixed in our tests, even though fewer images could be used to resolve the MEP and find the saddle point at lower computational cost. Using the same philosophy as applied to optimizer parameters, we want to use a conservative number of images that would identify intermediate minima between nearby initial and final states. The limited resolution along the path will result in some deviation between the images and the true MEP. This is not a disadvantage because it does not change the reaction mechanism qualitatively. To find the MEP to arbitrary accuracy, a steepest descent path can be traced from the saddle point(s) to the minima along the path (see Sec. 2.9).

2.5 Optimization Methods

The NEB method uses force projections (see Eq. 2.1) to find the MEP. Optimization routines are responsible for moving the NEB along these forces to the MEP. The force projections place a limitation on the optimization methods used since the NEB forces ($\mathbf{F}^{\mathrm{NEB}}$) are not conservative. Optimizers used with the NEB should not rely on the forces being consistent with an object function, rather, they should follow $\mathbf{F}^{\mathrm{NEB}}$ until its magnitude drops below a specified criteria. Here, we consider five force-based optimizers: steepest decent (SD), quick-min (QM) [3], fast inertial relaxation engine (FIRE) [14], conjugate gradients (CG) [15, 16], and limited-memory Broyden-Fletcher-Goldfarb-Shanno (L-BFGS) [17].

All of the optimizers were constrained with a maximum allowed step size for each NEB image. A value of 0.2 Å was found to prevent wild steps in high force regions while not significantly limiting performance in well-behaved low force regions. This parameter could, in principle, be thought of as an adjustable parameter and even used to control an unstable optimizer, but we did not find this to be a good strategy. For stable optimizers, performance was insensitive to the maximum step size, and for an unstable optimizer, controlling it with the maximum step size would result in an inefficient method resembling steepest descents. For this reason, we left the maximum step size fixed for all tests.

2.5.1 Steepest Decents

The SD method follows the force vector from an initial configuration to a zero in the force. Given a configuration $\mathbf{R}_j$ at iteration j, the SD step moves to a new configuration

$$\mathbf{R}_{j+1} = \mathbf{R}_j + \alpha\,\mathbf{F}_j, \tag{2.5}$$

where $\mathbf{F}_j$ is the force, and α is an adjustable parameter. If α is chosen to be the inverse of the curvature along the step direction, the optimizer will step directly to the minimum along the $\mathbf{F}_j$ direction. To ensure stability of the method, α should be less than $1/k_{\text{max}}$ where k_{max} is the maximum curvature in the system.

The SD method is known to converge slowly in stiff systems [16]. Here, it is presented as the simplest optimizer to which better methods can be compared.

2.5.2 Quick-min

The QM optimizer improves upon the SD method by accelerating the system in the direction of the force, making the minimization more aggressive[3]. QM is a damped dynamics routine, where the damping parameter is replaced by a projection of the velocity along the force. The QM method can be coupled with a velocity Verlet algorithm [18], or as described here, with an Euler integrator.

1. Project the velocity in the direction of the force,

   $\mathbf{V}_j = \left(\mathbf{V}_j \cdot \hat{\mathbf{F}}_j\right) \hat{\mathbf{F}}_j.$

2. Zero the velocity if it is anti-parallel to the force,

   if $\mathbf{V}_j \cdot \hat{\mathbf{F}}_j < 0$ then $\mathbf{V}_j = 0$.

3. Take an Euler step,

   $\mathbf{V}_{j+1} = \mathbf{V}_j + \Delta t\, \mathbf{F}_j,$

   $\mathbf{R}_{j+1} = \mathbf{R}_j + \Delta t\, \mathbf{V}_j.$

2.5.3 Fast Inertial Relaxation Engine

Like QM, the FIRE algorithm takes dynamical steps and resets the velocity if the force and velocity are in opposite directions. In addition FIRE employs a variable time step algorithm. The main difference is that QM projects the velocity onto the force vector, whereas FIRE only projects a component of the velocity in the force direction, while maintaining momentum in other directions. Details of this method can be found in Ref. [14].

2.5.4 Conjugate Gradients

The CG method improves upon the SD method by following conjugate search directions instead of always following the force. The algorithm employed is the Polak-Ribière formula [15, 16].

1. Initialize the search direction along the force,

   $\mathbf{d}_0 = \mathbf{F}_0.$

2. Calculate the step size, λ, using a line-minimizer,

   $\mathbf{R}_{j+1} = \mathbf{R}_j + \lambda\, \mathbf{d}_j.$

3. Evaluate the new conjugate search direction,

   $\mathbf{d}_{j+1} = \mathbf{F}_{j+1} + \gamma\, \mathbf{d}_j,$

where $\gamma = \mathbf{F}_{j+1} \cdot (\mathbf{F}_{j+1} - \mathbf{F}_j)/|\mathbf{F}_j|^2$. In our implementation, a single Newton's method step was used to minimize the force along the search direction, $\mathbf{d}_i$, at each iteration. The derivative of the force along the search direction was evaluated with a finite difference step so that each CG iteration requires two force evaluations.

2.5.5 Limited-memory Broyden-Fletcher-Goldfarb-Shanno

The L-BFGS method is a quasi-Newton method that builds up information about the second derivatives during optimization, and uses this information to step towards the predicted harmonic minimum [17, 16]. Specifically, the inverse Hessian matrix, $\mathbf{H}^{-1}$, is constructed iteratively, starting from a diagonal matrix. The L-BFGS method can be used in two ways. First, similar to CG, a search direction,

$$\mathbf{d}_j = \mathbf{F}_j \mathbf{H}_j^{-1}, \tag{2.6}$$

is identified at each iteration, and a line minimizer is used to step along that direction,

$$\mathbf{R}_{j+1} = \mathbf{R}_j + \lambda\, \mathbf{d}_j. \tag{2.7}$$

This method is referred to as L-BFGS(line).

A second approach is to use $\mathbf{H}^{-1}$ directly to calculate the step,

$$\mathbf{R}_{j+1} = \mathbf{R}_j + \mathbf{F}_j \mathbf{H}_j^{-1}. \tag{2.8}$$

This method, which we call L-BFGS(hess), requires only one force call per iteration (instead of two for L-BFGS(line)) because there is no finite difference step to calculate λ. On the other hand, L-BFGS(hess) requires a more conservative value for the diagonal elements of the initial inverse Hessian. Values that are too large result in oscillatory or wild behavior, and values that are too small lead to slow optimization. Both flavors of the L-BFGS algorithm are tested here.

The L-BFGS method uses a memory of previous iterations to build the inverse Hessian. The number of iterations in the memory is a variable parameter. In all cases, we have used a value of 25, and found only small changes in performance as long as this value is set large enough (greater than 10), however a larger value for the memory stabilizes the optimizer for a poor initial $\mathbf{H}^{-1}$.

2.5.6 Global L-BFGS

We also tested a global version of L-BFGS (GL-BFGS) in which all images along the band are minimized with a single instance of the optimizer, instead of having an optimizer for each image [19, 6, 20]. In both the local and global L-BFGS methods, the images are optimized collectively, but in the GL-BFGS method, the inter-image interactions are included in the inverse Hessian. The dimensionality of this matrix is $3 \times N \times P$ in GL-BFGS, where 3 is the dimensionality of space, N is the number of atoms, and P is the number of images along the band. In the local (image-by-image) L-BFGS method, there are P matrices, each of dimension $3 \times N$. In the GL-BFGS method the configuration of the band and the force acting on it are described by the vectors,

$$\begin{aligned} \mathbb{R} &= (\mathbf{R}_1, \mathbf{R}_2, ..., \mathbf{R}_P), \\ \mathbb{F} &= (\mathbf{F}_1, \mathbf{F}_2, ..., \mathbf{F}_P). \end{aligned} \tag{2.9}$$

The optimizer then works the same as the L-BFGS using $\mathbf{H}^{-1}$ (for the entire band) to either directly calculate the optimization step in GL-BFGS(hess), or with a line minimizer to calculate the step size (λ) in GL-BFGS(line).

2.6 NEB Convergence

The convergence of the NEB with the different optimizers was tested using a model system (see Ref. [21] for details) of the rearrangement mechanisms of a heptamer island diffusion on a FCC(111) crystal surface. The

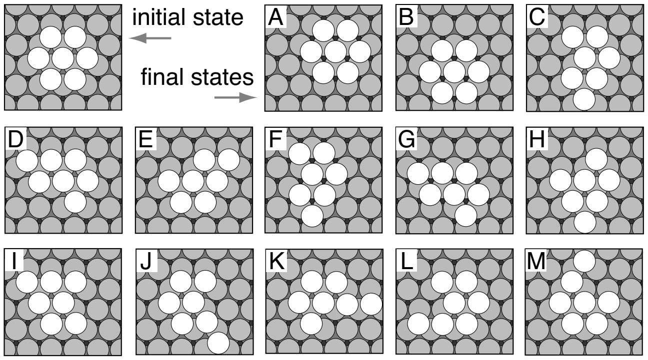

Figure 2.2: Low energy rearrangement processes for a heptamer island on a (111) surface. A pairwise Morse potential is used with parameters adjusted to model Pt.

surface was formed from six layers of a FCC crystal, with 56 atoms per layer and the three bottom layers held frozen in their equilibrium bulk positions. A seven atom heptagonal island was placed on the surface with each atom in hollow sites. Atomic interactions were described by a pairwise Morse potential,

$$V(r) = D_e \left[e^{-2\alpha(r-r_0)} - e^{-\alpha(r-r_0)} \right], \tag{2.10}$$

with parameters fit to Pt [22], $D_e = 0.7102$ eV, $\alpha = 1.6047$ Å^{-1}, and $r_0 = 2.8970$ Å. The potential was cut and shifted to zero at a distance of $r = 9.5$ Å.

Figure 2.2 shows the most stable initial state for the island and the thirteen product states with the lowest diffusion barriers. The NEB optimizers were tested by forming a linear band from the initial state to each final state and then counting the number of potential evaluations (force calls) required to reach convergence. Convergence was reached when the magnitude of the

Table 2.1: Average number of force calls to converge an eight image CI-NEB for heptamer island rearrangement with different optimizers. The NEB was considered converged when the magnitude of the force on each image dropped below the specified maximum force, satisfying: $\max \left|\mathbf{F}_i^{\text{NEB}}\right| < \text{F}_{\text{max}}$.

Optimization method	Force calls to reach F_{max} (eV/Å) of	
	0.01	0.001
SD: steepest descents	412	737
QM: quick-min	190	354
FIRE: fast inertial relaxation engine	77	116
CG: conjugate gradients	111	196
L-BFGS(line)	108	154
L-BFGS(hess)	351	428
GL-BFGS(line): global L-BFGS(line)	100	147
GL-BFGS(hess): global L-BFGS(hess)	49	73

force on all images was less than a specified maximum force, F_{max}, so that

$$\left[\mathbf{F}_i^{\text{NEB}} \cdot \mathbf{F}_i^{\text{NEB}}\right]^{1/2} < \text{F}_{\text{max}} \tag{2.11}$$

for each image i.

A comparison of the efficiency of the different optimizers with an eight image CI-NEB is presented in Table 2.1. The average number of force calls per image to reach force criteria, F_{max}, of 0.01 and 0.001 eV/Å, for the 13 processes illustrated in Fig. 2.2 are tabulated. Of the first order methods (SD, QM and FIRE), which do not explicitly calculate curvatures of the potential, SD is the least efficient. QM is better, but the recent modifications made in the FIRE algorithm result in a significantly more efficient algorithm for this system. The second order methods that use line optimizers (CG, L-BFGS(line) and GL-BFGS(line)) are slightly less efficient than FIRE. They require fewer iterations to converge, but each iteration involves two force evaluations to evaluate the curvature along a line by finite difference, so that the overall efficiency is lower. The Hessian based second order L-BFGS(hess) has the potential to be twice as fast as the line optimizer version, L-BFGS(line), but it is unstable when used with the NEB. The global version, GL-BFGS(hess), is stable and is half the cost of the GL-BFGS(line) method. This algorithm is 35% faster than FIRE, and the most efficient algorithm that we have tested for optimizing the NEB.

The instability of second-order algorithms when used with the NEB has been noted previously [23, 24], and associated with the NEB lacking a simple Lagrangian (or object function). The F^{NEB} forces are constructed with projections (see Eq. 2.1), resulting in non-conservative forces and a non-Hermitian Hessian matrix [24]. In this respect, optimizers that rely on curvature information could be inefficient or unstable when used with the NEB, but it is not well-understood why some optimizers have stability problems and others do not.

To better understand the interaction of the optimizers and the NEB, we compared the performance of each for NEB optimization with geometry minimization. Minimization is based upon conservative forces, so problems due to the non-conservative NEB forces should show up in the comparison. To make the minimization and NEB calculations as similar as possible, we minimized a geometry from the midpoint of each heptamer rearrangement

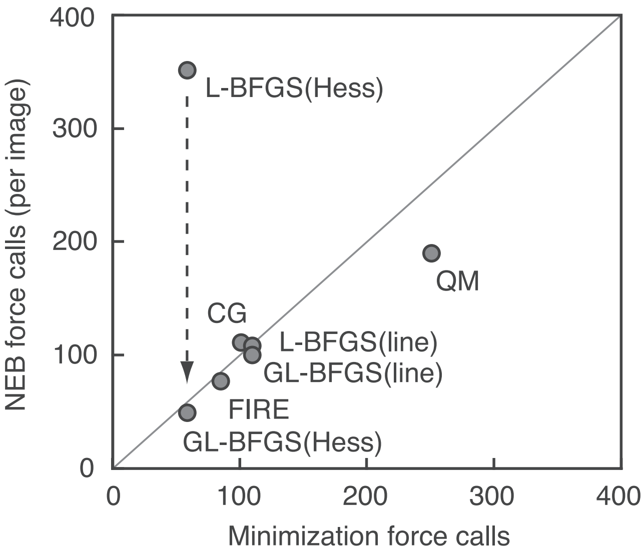

Figure 2.3: Optimizer performance with the NEB as compared to minimization. Points on the line indicate that it takes the same average number of force calls to minimize from the midpoint of each heptamer rearrangement process as it does for an image in the NEB to converge to the MEP (with F_{max} = 0.01 eV/Å). In general, the optimizers have a similar performance with the NEB as with minimization, and the second order methods (CG and L-BFGS) are better than the commonly-used QM algorithm. The FIRE algorithm is also a significant improvement over QM. The Hessian based L-BFGS is twice as fast as the line optimizer version, but only when optimization is done globally for the NEB.

process (see Fig. 2.2) and compared the average number of force calls required to reach $F_{max} = 0.01$ eV/Å, with the number of force calls (per image) required to converge the NEB with the same force criteria.

Figure 2.3 shows that the optimizer performance is very similar for the NEB and minimization calculations, with the notable exception of the L-BFGS(hess) optimizer. This optimizer works well for a single image, but is

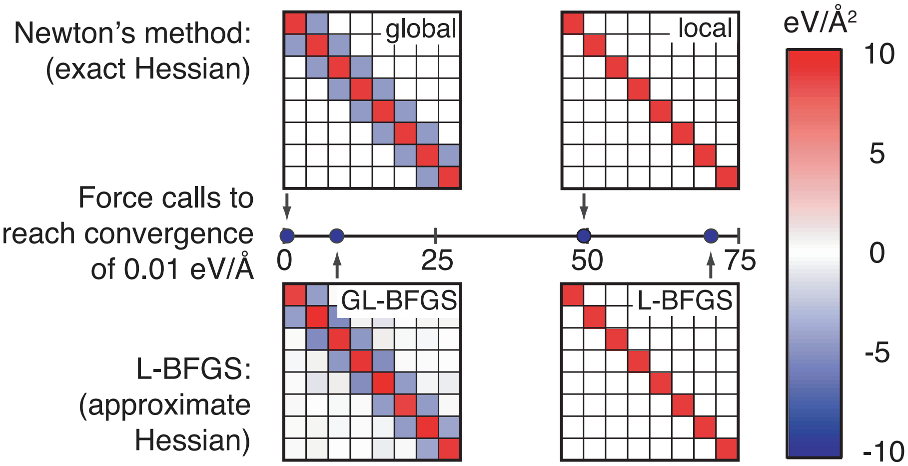

Figure 2.4: Number of iterations required to converge a string of images connected by springs on a line. The L-BFGS and GL-BFGS optimizers are compared to Newton's method, using Hessian matrices from both a local (image-by-image) and global (entire band). In this harmonic system, Newton's method with the global Hessian converges in one iteration, and GL-BFGS learns the full Hessian and converges in eight iterations. When these optimizers are restricted to local (diagonal) Hessian matricies, both are inefficient. This indicates that the GL-BFGS optimizer is more efficient than the L-BFGS method because it learns information about the inter-image (off-diagonal) elements of the Hessian.

unstable when used with the NEB. There is, however, a simple solution in the GL-BFGS(hess) optimizer. The use of a global inverse Hessian for the entire NEB, in which inter-image interactions are included, stabilizes the method and results in our most efficient optimizer.

The improved efficiency of GL-BFGS over the L-BFGS optimizer can be understood by looking at the Hessian matrices that each method constructs, and comparing them to Newton's method which uses the true Hessian of the system. To make this comparison, we use a simple system in which eight colinear images are connected by springs of strength $k = 5$ eV/Å^2. The exact global Hessian for this system, shown in Fig. 2.4, has values of $2k$ on the diagonal, and $-k$ on the off-diagonal elements. This is a harmonic system, so this exact Hessian is independent of geometry, and Newton's method converges in a single iteration. Newton's method can also be applied locally (image-by-image). Here, the Hessian for each image is the single value of $2k$, and the local Newton's method step is made by using a global Hessian solely with this value on the diagonal. Since this is not the exact Hessian for the full system, Newton's method takes longer (48 iterations) to converge.

The same comparison is made for L-BFGS and GL-BFGS. The L-BFGS is a local method (image-by-image), so it learns only the diagonal elements of the Hessian. It takes several iterations to learn this Hessian, and converges in 69 iterations - similar to the local implementation of Newton's method. The GL-BFGS optimizer is able to approximate the global Hessian, which is nearly identical to the exact Hessian by the time it converges in eight iterations (see Fig. 2.4). The off-diagonal elements of the Hessian are important for the global optimization of the band, and when they are included, the optimizer is significantly more efficient.

Beads on a line connected by springs is a simplified problem because the force projections of a NEB in higher dimensions are not present. Figure 2.5 shows a comparison of the final global Hessian for an eight image NEB on the two-dimensional LEPS potential coupled to a harmonic oscillator [3] (see

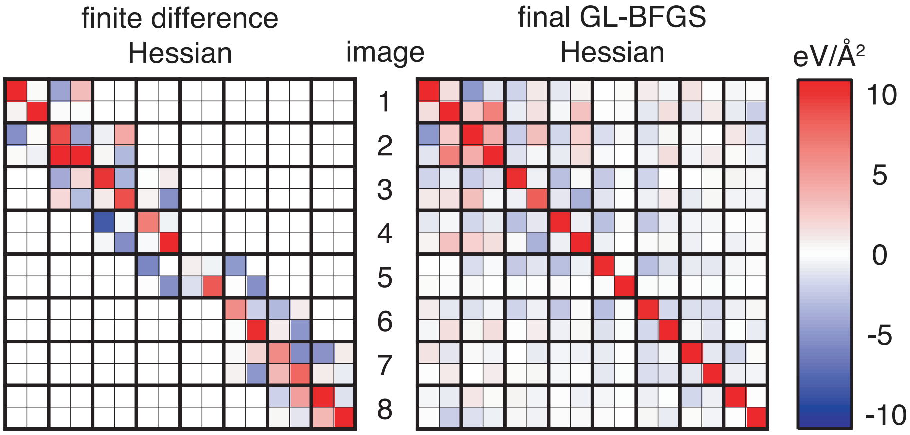

Figure 2.5: The exact (finite difference) Hessian for an eight image converged NEB on the two-dimensional LEPS potential coupled to a harmonic oscillator, compared with the approximate Hessian constructed during a GL-BFGS optimization. The exact Hessian shows the curvatures due to the potential on the block diagonal elements, and the inter-image spring and tangent interactions on the off-diagonal. The non-Hermitian nature of the NEB forces is apparent from the asymmetry in this matrix. The approximate GL-BFGS Hessian is necessarily symmetric, and only picks up some of the tri-diagonal nature of the exact Hessian. These off-diagonal elements are quite important however; GL-BFGS converges 2.5 times faster than L-BFGS which only has the block-diagonal elements.

Fig. 2.9). The true Hessian, calculated at the converged NEB, is not hermitian since the forces are not conservative. One can see, however, the strong curvatures due to the potential on the block-diagonal. The spring and tangent interactions between images appear in the off-diagonal blocks. The climbing-image can be seen as the 5th image. Here, there there are no off-diagonal elements since displacements of the neighboring images do not induce forces on the climbing-image. This is why the climbing-image tends to converge faster than other images when local optimizers are used. The GL-BFGS optimizer is forced to build up a symmetric Hessian. The (large) diagonal elements are similar to the true Hessian, and inter-image interactions are present, but the final Hessian differs significantly from the finite-difference Hessian. Clearly these inter-image elements are important, since GL-BFGS converges the NEB 2.5 times faster than the L-BFGS optimizer, but the qualitative error in the GL-BFGS Hessian suggests that the method could be further improved.

Finally, it should be noted that the line-optimizer based methods (CG and L-BFGS(line)) do not suffer from the same instability seen in L-BFGS(hess). In these methods, the line is chosen based upon local information, but the curvature along the line is found by finite-difference - globally for the entire NEB. This curvature is more accurate than predicted by the local (image-by-image) L-BFGS Hessian, and results in stable methods, although at roughly twice the cost of GL-BFGS(hess).

The fact that the stability of the L-BFGS optimizer is sensitive to how it is implemented could explain the conflicting reports about whether the method is unstable [23, 24] or not [6, 20] when used with the NEB and string methods. This later work, from the Wales group, used a global version of the L-BFGS method as implemented in their OPTIM code [19], and found it to be highly efficient for NEB calculations - which is consistent with what we find here.

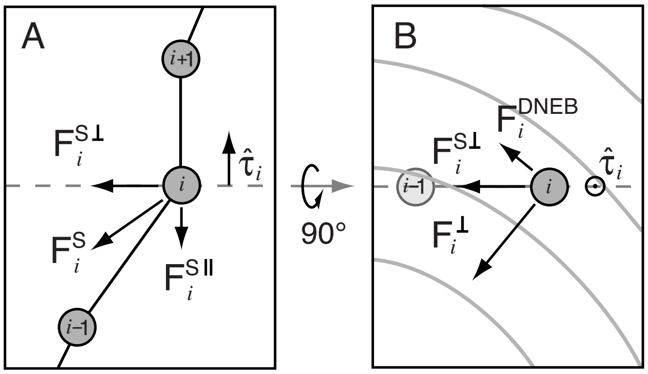

Figure 2.6: The doubly nudged elastic band includes an additional force, $\mathbf{F}_i^{\mathrm{DNEB}}$, to keep the band straight during convergence. This force is a component of the perpendicular spring force, $\mathbf{F}_i^{\mathrm{S}\perp}$, as shown in (A). The view in (B) is in the plane perpendicular to the band. Here $\mathbf{F}_i^{\mathrm{DNEB}}$ is shown as the component of $\mathbf{F}_i^{\mathrm{S}\perp}$ which is orthogonal to the perpendicular force due to the potential, $\mathbf{F}_i^{\perp}$.

2.7 Doubly Nudged Elastic Band

The NEB force projection restricts the potential forces to act perpendicular to the band, and spring forces along the band. Since these forces are orthogonal, there is no competition between the potential forces pointing images to the MEP and the spring forces keeping them equally spaced. Also, since the spring forces act only along the band, there is no tendency for the springs to shorten the band; the spring forces on each image go to zero when they are equally spaced.

Trygubenko *et al.* [6] proposed a double nudging modification to this projection scheme in which a component of the spring force acts perpendicular to the path. This component acts to straighten the band, keeping it shorter during convergence. Double nudging is very similar in spirit to the angular switching function introduced in the original NEB method [3] which was made unnecessary with an up-winding tangent [4]. The strength of the double nudging method is that it uses only the component of the perpendicular spring force which is not along the potential force, so that it does not cause corner-cutting [3]. Figure 2.6 illustrates this projection and the resulting double nudging force, $\mathbf{F}_i^{\mathrm{DNEB}}$, which is added to the i^{th} image in the NEB.

To write the double nudging force explicitly, we take the component of the spring force,

$$\mathbf{F}_i^{\mathrm{S}} = k\left[(\mathbf{R}_{i+1} - \mathbf{R}_i) - (\mathbf{R}_i - \mathbf{R}_{i-1})\right], \tag{2.12}$$

which is perpendicular to the tangent $\hat{\boldsymbol{\tau}}_i$,

$$\mathbf{F}_i^{\mathrm{S}\perp} = \mathbf{F}_i^{\mathrm{S}} - \mathbf{F}_i^{\mathrm{S}} \cdot \hat{\boldsymbol{\tau}}_i\, \hat{\boldsymbol{\tau}}_i. \tag{2.13}$$

Figure 2.6A illustrates the perpendicular and parallel components of the spring force, and Fig. 2.6B shows the plane normal to the tangent, $\hat{\boldsymbol{\tau}}_i$, at image i. The perpendicular potential force, $\mathbf{F}_i^{\perp}$, and the perpendicular spring force, $\mathbf{F}_i^{\mathrm{S}\perp}$, are both in this plane. The double nudging force, $\mathbf{F}_i^{\mathrm{DNEB}}$, is the component of $\mathbf{F}_i^{\mathrm{S}\perp}$ which is orthogonal to $\mathbf{F}_i^{\perp}$,

$$\mathbf{F}_i^{\mathrm{DNEB}} = \mathbf{F}_i^{\mathrm{S}\perp} - \mathbf{F}_i^{\mathrm{S}\perp} \cdot \hat{\mathbf{F}}_i^{\perp}\, \hat{\mathbf{F}}_i^{\perp}. \tag{2.14}$$

The addition of this force to all (non-climbing) images of the NEB is the doubly nudged elastic band (DNEB) [6].

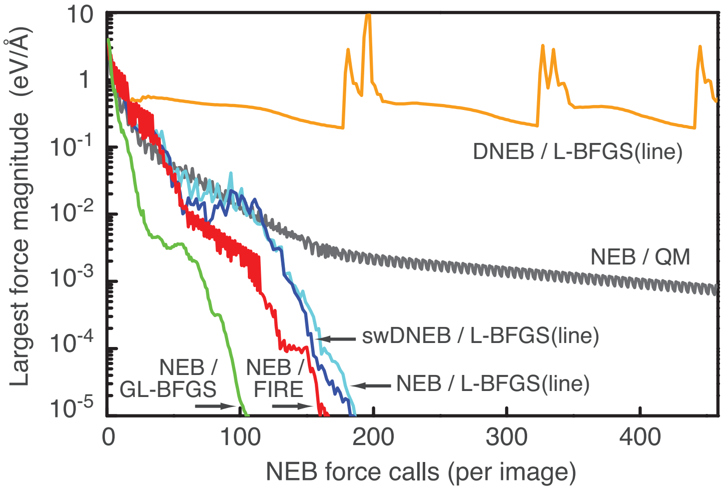

Figure 2.7: Convergence of the NEB and DNEB with different optimizers, for the Pt island rearrangement process illustrated in Fig. 2.2C. The DNEB has an instability at low force which prevents convergence. When the DNEB force is smoothly switched off during convergence (swDNEB), the performance is similar to the NEB. This plot also shows how the FIRE and GL-BFGS optimizers converge at a faster rate than QM.

Trygubenko *et al.* report that the addition of the double nudging force improves the stability of convergence with the NEB when using the L-BFGS optimizer [6]. They also mention that the DNEB cannot be used to accurately converge the MEP. The convergence problems are caused because the perpendicular spring force, $\mathbf{F}_i^{\mathrm{S}\perp}$ does not go to zero for a curved path, and is only projected out if it is parallel to the potential force, $\mathbf{F}_i^{\perp}$. Upon convergence, this perpendicular component of the potential force, $\mathbf{F}_i^{\perp}$, goes to zero, so it will not project out the double nudging force, and the band will feel a straightening force. This frustration is illustrated in Fig. 2.7. The DNEB method can only converge the NEB to 0.2 eV/Å before it gets knocked away from MEP by the double nudging force.

The DNEB method was shown to work well when applied to long pathways with high initial forces [6, 20] which is not the conditions under which are testing it. To improve the convergence of the DNEB at lower forces, we introduced a switching function which turns off $\mathbf{F}_i^{\mathrm{DNEB}}$ as the NEB converges and the magnitude of $\mathbf{F}_i^{\perp}$ drops below that of the spring force, $\mathbf{F}_i^{\mathrm{S}\perp}$,

$$\mathbf{F}_i^{\mathrm{swDNEB}} = \frac{2}{\pi} \tan^{-1} \left[\frac{|\mathbf{F}_i^{\perp}|^2}{|\mathbf{F}_i^{\mathrm{S}\perp}|^2} \right] \mathbf{F}_i^{\mathrm{DNEB}}. \tag{2.15}$$

Figure 2.7 shows the improved stability of this switched DNEB method (swDNEB), but also shows that it does not improve convergence over the regular NEB. It would be interesting to see if this method improves the stability of NEB calculations with high forces and also allow for accurate convergence, but such a test is beyond the scope of this work.

2.8 String Method

The idea behind the string method is that a continuous reaction pathway (string) is optimized to the MEP [7]. Practically, however, the string method is very similar to the NEB in that the pathway is represented by a set of images connected by linear segments. The same tangent and force projections in the NEB [4] are used to direct the images along the string to the MEP. A climbing image [5] can also be used to find the saddle point precisely. The main difference between the string and NEB methods is how the images are kept equally spaced along the pathway (or by some other specified dis-

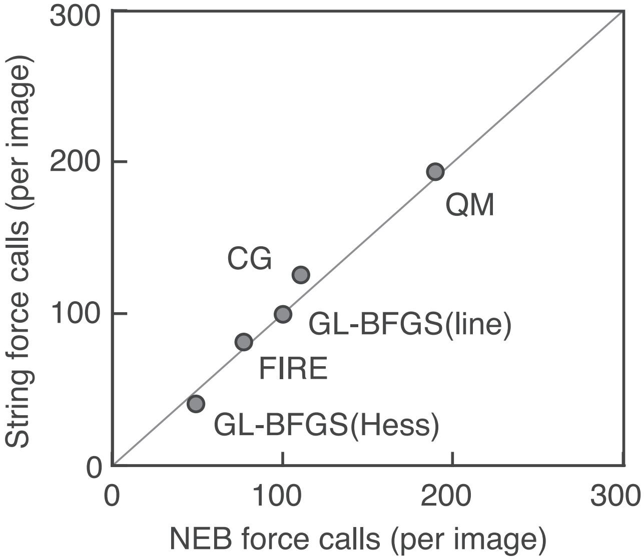

Figure 2.8: Number of force calls required to converge the string and NEB methods to a force criteria of 0.01 eV/Å with different optimizers. The linear trend shows that the performance of the NEB and string method (using the NEB up-winding tangent) are the same, and that GL-BFGS is the most efficient optimizer.

tribution). In the NEB method, spring forces are introduced between images along the band, and the optimizer ensures equal spacing by minimizing these forces. In the string method, no spring forces are used. Instead, the images are kept equally spaced by repositioning them equally along the path after each iteration. Since the path is defined by the images, the repositioning step gives equal spacing to first order. Despite these different approaches for distributing images along the path, we find that there is no significant difference in the final path, or the rate at which the methods converge. Figure 2.8 shows that it takes the same amount of work to converge the string and NEB method with each optimizer. Either the NEB springs or the string re-distribution can be used with the optimizers to efficiently find the MEP. These results are consistent with another recent study finding that the NEB and string methods have similar performance when calculating isomerization pathways in small clusters and for folding pathways in peptides [25]. What is important for these methods is the definition of the tangent along the path, the force projections, and the climbing-image method for finding the saddle point.

2.9 Simplified String Method

Recently, W. E *et al.* proposed a simplified version of the string method [8]. This method is described as being simpler than the NEB and string methods because it does not require a definition of the tangent along the path or the use of force projections. Instead, a cubic spline is used to parameterize the pathway between images. At each iteration, images are moved down the force, and then redistributed along the spline. Convergence is based upon how far the images move after each full iteration.

We have done two tests to compare the NEB and the simplified string method. First, we compare the accuracy of the methods, by calculating the root-mean-squared (RMS) distance between the images on the converged bands and the true MEP. For this test we used a LEPS potential coupled to a harmonic oscillator to form a two-dimensional potential energy surface [3]. Figure 2.9 shows this RMS-distance as a function of the number of images used in each method. We find two separate regimes; with more than 25 im-

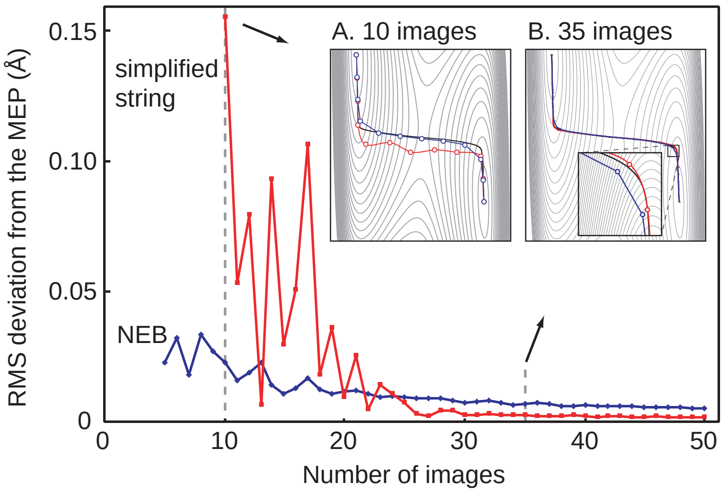

Figure 2.9: Accuracy of the simplified string and NEB, measured by comparing the root-mean-squared (RMS) deviation to the true MEP as a function of the number of images used to represent the path. For more than 25 images, the simplified string with a cubic spline interpolating function is closer to the MEP than the NEB with a one-sided up-winding tangent (B). Between 10 and 25 images, the simplified string develops oscillations and tends to deviate further from the MEP than the NEB method (A). With fewer than 10 images, the simplified string is unstable and does not converge. In this regime, the NEB remains stable, and is the preferred method.

ages the string method more accurately reproduces the MEP, and with fewer the string becomes unstable and the NEB is more accurate. The insets illustrate what is happening in these two regimes. Inset B shows how the string method follows the true MEP more closely than the NEB at a high-curvature region of the path. This is consistent with the findings of W. E *et al.*, that the simplified string reproduces the MEP to higher order than the NEB, and will follow it more closely in the limit of many images [8]. In the 10-25 image range, the simplified string is poorly behaved and converged to a path that oscillates around the MEP (see inset A). With fewer than 10 images, the simplified string oscillates without converging. We attribute this instability to the fact that the simplified string does not use an up-winding tangent. Tests (not presented here) show that the simplified string becomes unstable at the same point that a central-difference tangent becomes unstable, so we believe that the instability has the same root cause that is described in Ref. [4].

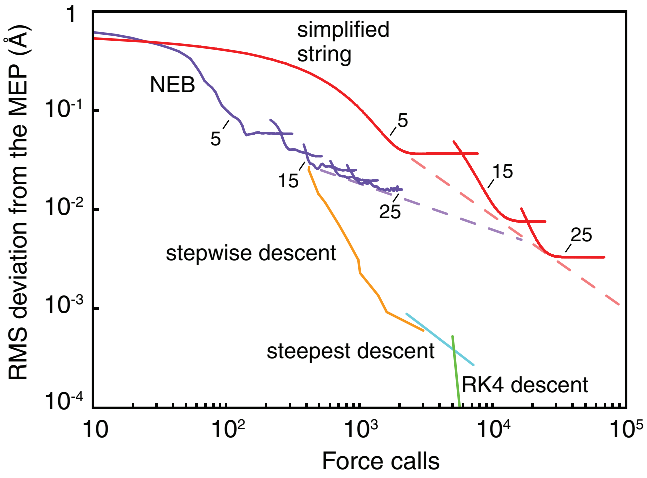

Figure 2.10: The accuracy of MEP finding methods as a function of computational cost. The process chosen for this comparison is the Pt island rearrangement illustrated in Fig. 2.2C. Accuracy is measured as the RMS distance between the images of each method and the true MEP. Cost is measured by the total number of force evaluations. Two types of approaches are compared - the NEB and simplified string, chain-of-states methods, and methods which require finding the saddle first before minimizing down the MEP via a stepwise, steepest, or RK4 descent trajectory. For calculations with 25 images or less, the NEB is more efficient than the simplified string. For accurate calculations with more than 10^4 force calls, the simplified string becomes more efficient because it is based upon the higher-order (RK4) optimizer and (cubic spline) interpolation between images. However, this is not as efficient as first finding the saddle (here with a five-image CI-NEB calculation) and then descending along the MEP. In this test, one should switch to a saddle-then-descend approach instead of using a 15 or greater image NEB.

Using the RMS distance to the MEP as a measure of accuracy illustrates a strength of the higher order interpolation used in the simplified string method as compared to the NEB when the path is represented by many images. As discussed in Sec. 2.4, however, this is not typically important for calculations of chemical rates. Taking Fig. 2.9B as an example - as long as both the simplified string and NEB include a climbing-image to find the saddle, they describe the rate and mechanism of reaction equally well. Furthermore, once the saddle point is found, it is a simple calculation to descend from the saddle along the MEP.

The computational cost of calculating an MEP to arbitrary accuracy with the simplified string and NEB was compared for the Pt(111) island rearrangement process shown in Fig. 2.2C. The accuracy of both methods is limited by the number of images used, so we performed tests with increasing numbers of images (5, 15, and 25) to compare the methods. The GL-BFGS optimizer was used for the NEB calculations and the fourth order Runga-Kutta (RK4) integrator with an optimized time-step for the simplified string. RK4 is the suggested method for moving images down the force in the simplified-string method [8]; the other optimizers discussed in this paper either cannot be used since the forces do not go to zero upon convergence, or they are not as efficient as RK4.

Figure 2.10 shows how the accuracy of the NEB and simplified string methods compare. The blue (NEB) and red (simplified-string), curves labeled with "5," both have five images. The curve shows the accuracy of the images as they converge. Eventually, both curves plateau as the methods reach an intrinsic error due to the finite resolution of the bands. The higher accuracy of the simplified-string can be seen by the smaller plateau value, but also that it is reached only after many more force calls. As more images are used, both methods become more accurate with an increasing cost. The dashed lines indicate the order of the methods - the NEB is of lower order since it uses a single sided tangent approximation, as compared to the cubic spline in the simplified-string method, so eventually it is more efficient to use the simplified string method. This is consistent with the findings of W. E *et al.* [8].

There is, however, a more efficient approach to finding highly accurate MEPs. Once the saddle point(s) is found the MEP can be followed by descending from the saddle(s) to the minima. The saddle point(s) can be found with arbitrary accuracy using a climbing-image NEB calculation with a minimal number of images, or using a min-mode following method [12, 13, 26]. Here we used a five-image CI-NEB to find the saddle, and then the dimer method to find the lowest mode at the saddle [12], along which a descent trajectory is started. The cost of finding the saddle and the lowest mode was 203 force calls.

Several descent methods were used to trace out the MEP. A relatively inexpensive method, described here as stepwise descent, finds the next image that is a fixed distance down the MEP. The force on this next image is minimized using the quick-min optimizer until the force perpendicular to the path drops below a specified value. This method was repeated for increasingly higher path resolutions (with higher accuracy and cost) to trace out the orange line labeled 'stepwise descent' in Fig. 2.10. At a cost of 3×10^3 force calls, the stepwise descent method becomes comparable to the steepest descent method which takes steps down the MEP in proportion to the force. Steepest descents is only stable for α below 0.04 eV/Å^2, so the stepwise descent is a good intermediate solution for tracing out the MEP for this potential. Finally, for even higher accuracy, the RK4 method is used to trace out the MEP. Here a maximum time step of 0.55 fs could be used. Smaller time steps rapidly increased the accuracy of the MEP, making this the most efficient method for finding MEPs with an error smaller than 10^{-4} Å.

2.10 Density Functional Theory Calculations

Computational efficiency is particularly important for finding reaction pathways when atomic interactions are based upon first-principles calculations. The methods compared here require forces and energies, which are available from density functional theory (DFT) calculations. Here we test our results of Sec. 2.6 on two systems with very different kinds of atomic interactions, described by DFT: the diffusion of a Pd tetramer on the MgO(100) oxide surface [27], and the dissociative adsorption and diffusion of oxygen on Au(111).

Our DFT calculations are performed with the Vienna Ab initio Simulation Package, VASP. Electronic wavefunctions are described with a plane-wave basis set. Exchange and correlation are modeled with the PW91 generalized gradient approximation (GGA) functional [28]. Ultra-soft pseudopoten-

Table 2.2: Number of force calls required to converge a five image CI-NEB for three different reaction mechanisms described by DFT. In each case, our GL-BFGS(hess) optimizer outperformed existing methods, although this was particularly clear for the diffusion processes (I and III). Breaking of the stiff O-O bond in process II requires a conservative initial Hessian for the GL-BFGS method, which limited its convergence rate as compared to the damped dynamics methods. The NEB was considered converged when the magnitude of the force on each image dropped below 0.01 eV/Å.

Process	QM	FIRE	GL-BFGS
I. Pd_4 diffusion on MgO(100):	178	148	98
II. O_2 dissociation on Au(111):	187	147	126
III. O diffusion on Au(111):	59	128	33

tials of the Vanderbilt form [29] are used to smooth the wavefunctions within the core atomic regions, and these wavefunctions are orthogonalized to a frozen core within the projector augmented wave (PAW) framework [30]. A plane-wave cut-off of 250 eV was set appropriate for the pseudopotentials. In the MgO oxide system, a single Γ-point calculation was sufficient for sampling the Brillouin zone, and for the Au surface, a 4×4×1 Monkhorst-Pack mesh [31] was used.

2.10.1 Pd_4 Diffusion on MgO(100)

The MgO(100) surface is modeled with three layers, each with 36 atoms. The bottom two layers are frozen in bulk lattice sites and the top layer is relaxed to accommodate surface interactions. The diffusion process investigated is a Pd tetramer rolling over one edge to a mirrored final state (see Fig 2.11). The optimizers show the same performance trend as in Sec. 2.6, with GL-

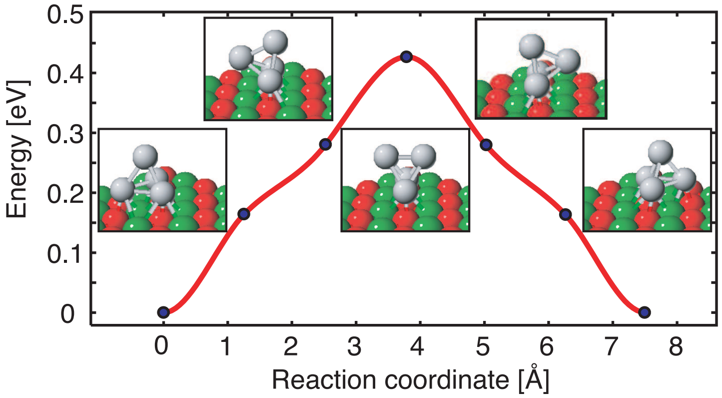

Figure 2.11: A Pd_4 cluster diffuses by rolling on the MgO(100) surface. Grey atoms are Pd, red are O, and green are Mg.

BFGS out-performing the standard QM algorithm by a factor of 2. It should be noted here, as stated in Sec. 2.4, that the optimizer parameters were not optimized specifically for the system; rather, default values were used. For QM and FIRE a time step of 0.10 (in 10.18 fs units) and for GL-BFGS the initial diagonal $\mathbf{H}^{-1}$ was scaled to have an inverse curvature of 0.05 $Å^2/eV$.

2.10.2 O_2 Dissociation and Diffusion on Au(111)

The dissociative adsorption of O_2 on Au(111) was calculated to test our results on a system with a strong covalent bond. The Au(111) surface was modeled as a four layer slab with nine atoms per layer and the top two layers relaxed. This reaction is qualitatively different from both the heptamer Pt island rearrangement processes and the Pd tetramer rollover process because of large variance in bond strengths. To converge the NEB with GL-BFGS(hess), a reduced scaled $\mathbf{H}^{-1}$ of 0.01 $Å^2/eV$ was necessary. For stability, this must

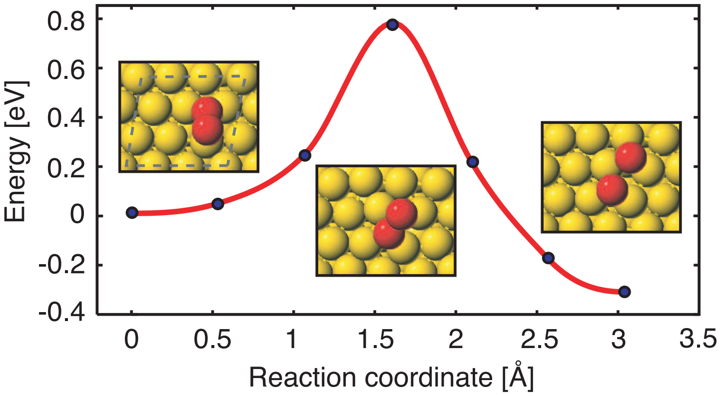

Figure 2.12: Reaction mechanism of O_2 dissociative adsorption on Au(111) into adjacent fcc hollow sites.

be set smaller than the inverse of the stiffest mode. The O-O stretch mode is calculated as 48.1 eV/Å^2, requiring an initial scaling of $\mathbf{H}^{-1}$ smaller than 0.02 Å^2/eV.

To verify that the lower GL-BFGS performance (only 15% faster than FIRE) is due to the stiff O-O mode and conservative $\mathbf{H}^{-1}$, we choose a second processes involving O diffusion on the Au(111) slab (see Fig. 2.13). Here, the highest curvature is 9.4 eV/Å^2, which is small enough to use our more aggressive $\mathbf{H}^{-1}$ value of 0.05 Å^2/eV. As shown in Tab. 2.2, the performance gap between GL-BFGS and QM/FIRE increases, similar to what we found for the Pd tetramer and Pt island rearrangement systems.

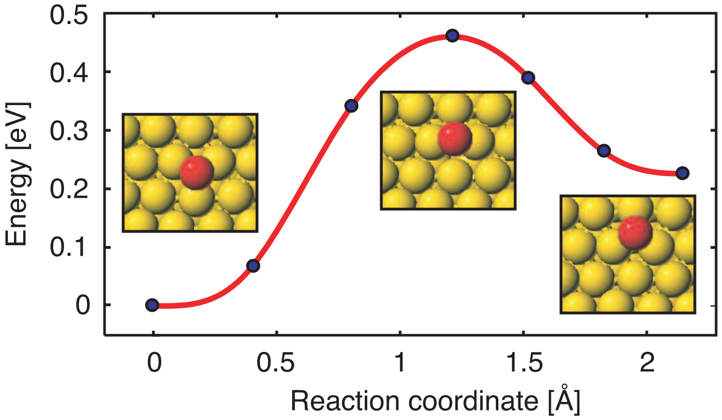

Figure 2.13: Diffusion of O between hollow sites on Au(111)

2.11 Discussion

In our comparison of different methods, we have chosen a few test systems, a convergence criteria, and a limited number of optimizers. By making these choices, there is a danger of omitting methods, optimizers, or focusing on types of systems that do not emphasize the strengths and weaknesses of different approaches. Some of the methods that have not been compared here are the adaptive NEB [23], the super-linear minimization scheme for the NEB [24], the growing string [32], the quadratic string method [33, 34], and a combination of double and single ended searches [4, 6].

Direct comparisons between methods is made easier when tests are made on easy-to-implement benchmark systems (such as the pairwise Morse potential used here) and when the code for algorithms is made available. To facilitate such comparisons in the future, the codes used for the calculations in this manuscript are available at Ref. [35].

2.12 Conclusions

Our comparison of methods for finding minimum energy paths shows that the when the same force projection and tangent definition is used, the method by which images are kept equally spaced (springs in the NEB method or redistribution with the string method) does not have a significant impact on computational efficiency; the optimizer is more important. Here we show that a global implementation of the L-BFGS method, in which inter-image curvatures are included in the memory of the optimizer, is the most efficient approach. Also, we show that the FIRE optimizer tends to be more efficient than quick-min, and is the preferred optimizer that does not (explicitly) rely on curvature information. Both the NEB and string methods can incorporate a climbing-image to efficiently find a saddle point while using as few images as possible to represent the MEP. To find a high accuracy MEP, it is more efficient to first find the saddle and then descend to minima, as compared to using a chain-of-states method (NEB, string, or simplified string) with many images. All methods compared are force-based and can be used with DFT calculations. The most efficient methods have been shown to work well both for empirical pair-wise potentials and for metal-oxide and covalent bond breaking reactions at surfaces as described by DFT.

2.13 Acknowledgments

We would like to thank David Wales and Andri Arnaldsson for helpful comments and suggestions. This work was supported by the National Science Foundation from an NSF-CAREER award (CHE-0645497), the Robert A. Welch Foundation, award No. F-160, and the Texas Advanced Computing Center at the University of Texas at Austin.

Chapter 3

Paths to which the nudged elastic band converges

3.1 Abstract

A recent letter to the editor [W. Quapp and J. M. Bofill, J Comput Chem 31, 2526, (2010)] claims that the nudged elastic band (NEB) method can converge towards gradient extremal paths and not to steepest descent paths, as has been assumed. In this letter, we show that the NEB does converge to steepest descent paths, and that the observed tendency for the NEB to approach gradient extremal paths was a consequence of implementation errors. We clarify while the NEB finds steepest descent paths, these are not necessarily minimum energy paths in the sense of being a set of points which are minima in the potential energy surface perpendicular to the path. Segments of steepest descent paths can also follow potential energy ridges.

3.2 Abstract

A recent letter to the editor [W. Quapp and J. M. Bofill, J Comput Chem 31, 2526, (2010)] claims that the nudged elastic band (NEB) method can converge towards gradient extremal paths and not to steepest descent paths,

as has been assumed. In this letter, we show that the NEB does converge to steepest descent paths, and that the observed tendency for the NEB to approach gradient extremal paths was a consequence of implementation errors. We clarify while the NEB finds steepest descent paths, these are not necessarily minimum energy paths in the sense of being a set of points which are minima in the potential energy surface perpendicular to the path. Segments of steepest descent paths can also follow potential energy ridges.

3.3 NEB and Steepest Decent Paths

The nudged elastic band (NEB) is a method to find steepest descent (SD) paths between stable states on a potential energy landscape. [3, 5, 4] The path is discretized into a set of images and each image i is subjected to projected forces,

$$\mathbf{F}_i^{\mathrm{NEB}} = \mathbf{F}_i^{s\parallel} + \mathbf{F}_i^{g\perp}. \tag{3.1}$$

where $\mathbf{F}_i^{s\parallel}$ are spring forces that act parallel to the path $\hat{\boldsymbol{\tau}}_i$,

$$\mathbf{F}_i^{s\parallel} = k\left(|\mathbf{R}_{i+1} - \mathbf{R}_i|^2 - |\mathbf{R}_i - \mathbf{R}_{i-1}|^2\right)\hat{\boldsymbol{\tau}}_i \tag{3.2}$$

and $\mathbf{F}_i^{g\perp}$ are the forces due to the potential that act perpendicular to the path,

$$\mathbf{F}_i^{g\perp} = \mathbf{F}_i - (\mathbf{F}_i \cdot \hat{\boldsymbol{\tau}}_i)\,\hat{\boldsymbol{\tau}}_i\,. \tag{3.3}$$

Here, $\mathbf{F}_i = -\nabla V(\mathbf{R}_i)$ is the negative gradient of the potential at image i, $\hat{\boldsymbol{\tau}}_i$ is the local tangent to the path, and k is a spring constant which is used to keep the images equally spaced along the path.

When the NEB forces are followed by an appropriate optimizer, such as those described in Ref. [36], convergence is reached when all images lie on a SD path. The SD path is precise in the limit of many images. A proof of this follows from considering the conditions when the NEB forces vanish. When the parallel force from Eq. 3.2 is zero, the images are equally spaced,

$$|\mathbf{R}_{i+1} - \mathbf{R}_i| = |\mathbf{R}_i - \mathbf{R}_{i-1}|\,, \tag{3.4}$$

independent of the choice of spring constant k. When the perpendicular force is zero, Eq. 3.3 reduces to

$$\mathbf{F}_i = (\mathbf{F}_i \cdot \hat{\boldsymbol{\tau}}_i)\,\hat{\boldsymbol{\tau}}_i\,, \tag{3.5}$$

showing the tangent $\hat{\boldsymbol{\tau}}_i$ to the path at each image i is parallel to the force at that image, $\mathbf{F}_i$. This is the definition of a SD path.

In Ref. [37], the authors claim the NEB does not converge to a SD path, but rather converges towards a different kind of path called a gradient extremal (GE). A GE path is one containing a set of points in which the derivative of the potential is parallel to a normal mode. A GE path does not generally follow the gradient; it has a greater tendency to follow ridges and valleys.

The example cited in Ref. [37] is an NEB calculation on the NFK potential as modified by Hirsch. [38] Figure 3.1 shows SD and GE paths leading from a saddle point to a minimum on the potential energy surface. With the NEB implementation used by the authors in Ref. [37], an initial linear band is

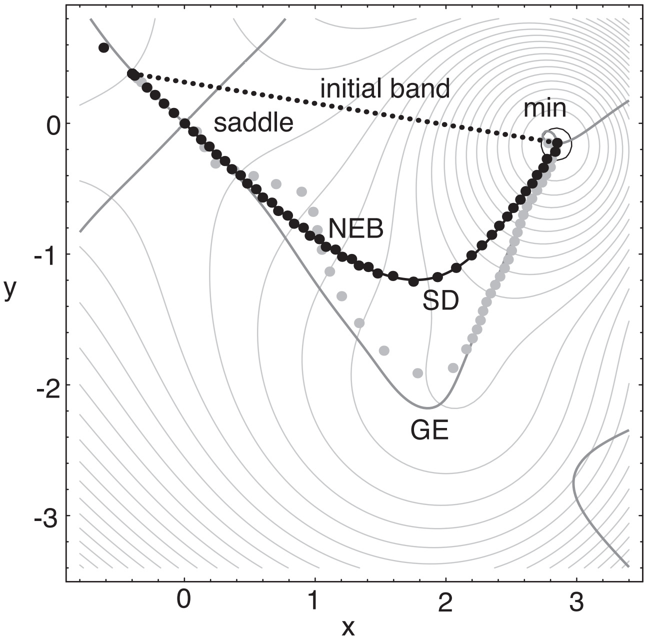

Figure 3.1: The grey points are the result of an NEB calculation described in Ref. [37], in which an initial (linear) band converges towards a GE path. When the minimizer is corrected, the NEB is properly converges to a SD path.

seen to converge towards a GE. The reason the NEB did not converge to the SD path is due to a coding error in the damped-dynamics optimizer whereby sequential images along the NEB would accumulate the velocity of previous images. When the code was corrected the NEB was shown to converge to the SD. The unequal spacing of the images in the converged NEB is due to a choice of k=0 in Ref. [37]. A more accurate path would be found using the standard implementation of the NEB described in Ref. [5], with springs to keep the images equally spaced and an upwinding tangent to avoid oscillations in steep sections of the path. Two other changes would improve this calculation: fewer

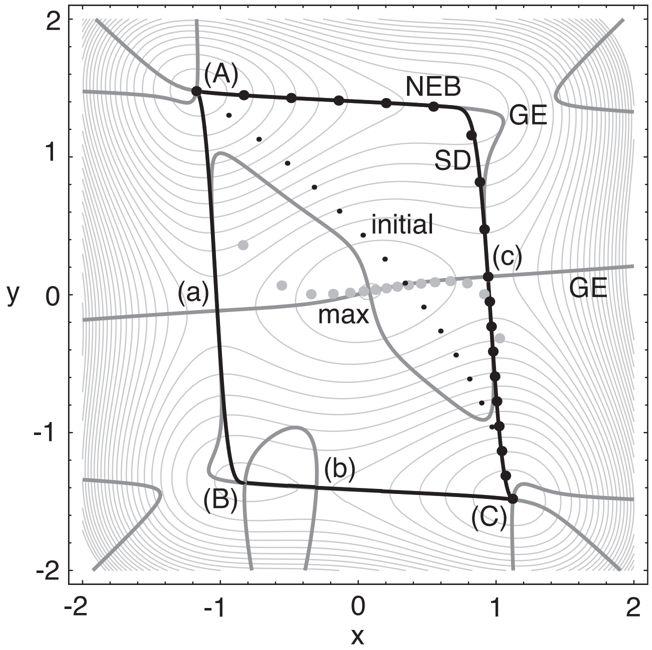

Figure 3.2: An NEB calculation described in Ref. [39] from minimum (A) to (C) on the WQ potential was shown to follow a ridge between saddle points (a) and (c) through a maximum along a GE path. When an error in the potential gradient is corrected, the NEB properly converges to a SD path through saddle (c).

images are required to identify the saddle point with the climbing image NEB, [4] and second-order optimizers increase the rate of convergence. [36]

A second example, cited in Ref. [37], of the NEB failing to converge to a SD path is shown in Fig. 3.2. The authors refer to a calculation on the Wolfe-Quapp (WQ) potential, detailed in Fig. 5 from Ref. [39], in which the NEB was found to converge towards a ridge and pass through the maximum. Only five optimization steps were possible before this calculation diverged. Again, a review of the code used for this calculation revealed implementation errors. The same integrator problem described previously was present in this code, but also, the sign of the y component of the force was incorrect so the ridge appeared to the NEB as a valley. Figure 3.2 shows a properly converged NEB to a SD path passing through saddle point (c), calculated using a corrected version of the code.

3.4 Steepest decent and minimum energy paths

In one regard, the authors of Ref. [37] bring up an important point about the NEB which has not been widely addressed in the literature. It is commonly assumed the NEB finds a minimum energy (ME) path, even though this is not always the same as a SD path. A SD path is one which follows the gradient, and a ME path is one in which the energy is also a minimum perpendicular to the path.

To show an example where the NEB finds a SD path which is not a ME path, we have constructed a periodic potential containing two Gaussian hills,

$$\cos(\pi x) + \cos(\pi y) + \pi e^{-\pi x^2}\left[e^{-\pi(y-0.8)^2} + e^{-\pi(y-0.8)^2}\right].$$

A contour plot of this potential is shown in Fig. 3.3. The ME path from the highest energy saddle point (e) terminates at nearby inflection points, where the path crosses the GE. The SD path continues on to saddle points (a) and (c) and then to minima (A) and (D). A converged NEB is shown to follow the SD path along the valley, where it is also a ME path, but also along a

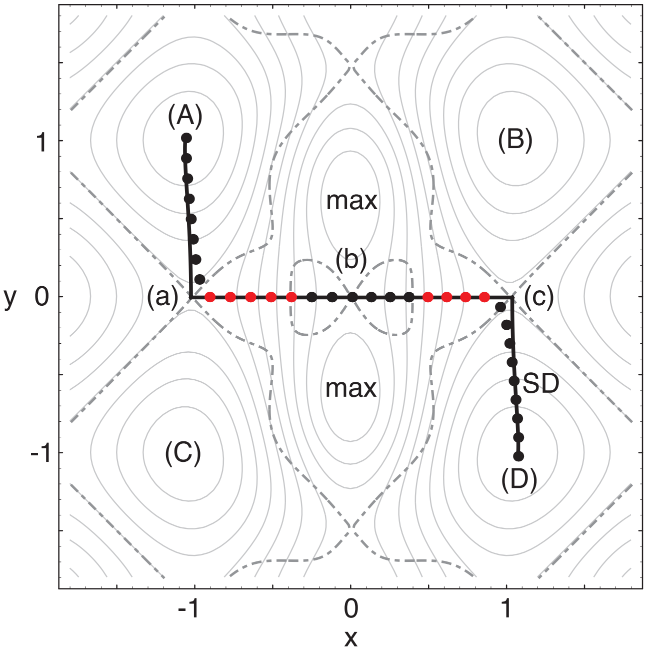

Figure 3.3: The SD path (solid black) from the highest energy saddle (b) terminates at minima (A) and (D) after passing through intermediate saddles (a) and (c), respectively. The images in red are where the NEB converges to a ridge along the SD path, which is not a ME path. The dashed line is the boarder between convex and concave reagons.

ridge where the energy is a maximum perpendicular to the path. The NEB will follow such paths in the limit of many images, but it will become unstable when $|C| = |\mathbf{F}|/\Delta\mathbf{R}$, where C is the negative curvature perpendicular to the ridge, $\mathbf{F}$ is the magnitude of the force down the ridge, and $\Delta\mathbf{R}$ is the image spacing. This analysis is closely related to stability analysis of the NEB in Ref. [5].

Finally, we show that the NEB can follow ridges in higher dimensional systems as well, and that this is not a pathology of low-dimensional potentials. An example is the diffusion of an Al adatom on the Al(110) surface, which has been studies by Tiwary and Fichthorn. [40] The adatom sits in a $(1\bar{1}0)$ channel on the surface, as shown in Fig. 3.3. Calculations of diffusion were done using the Vienna *Ab initio* Simulation Package using the PW91 GGA functional and the projector augmented wave method to treat core electrons. [30] valence electrons were described using a plane-wave basis with a cut-off energy of 250 eV. The adatom was placed on a p(4×3) cell with ten bilayers, freezing the bottom five to the bulk geometry. A vacuum gap of 15 Å separated the periodic images of the slabs, and a 6×6×1 Monkhorst-Pack mesh of was used to sample the Brillouin zone.

Fig. 3.4 shows the low energy mechanisms for cross-channel diffusion. The NEB calculation from minimum (A) to (D) converges along a ridge in a transition analogous to Fig. 3.3. The transition path in Fig. 3.4 climbs from minimum (A) up the the ME path to saddle point (a). Continuing on would lead to a diagonal cross-channel diffusion mechanism, to (C). Instead, the SD path from the higher energy saddle (b) [which is in fact a very shallow metastable minimum separated by two saddles] is followed by an NEB connecting to (D), resulting in a straight cross-channel diffusion mechanism. There are two ridge segments highlighted in red, one between (a) and (b), and a also between (b) and (c), are where the SD path is not a ME path.

In the limit of many images the NEB converges to the SD paths. The SD path is often an ME path, but this is not necessarily the case, for example

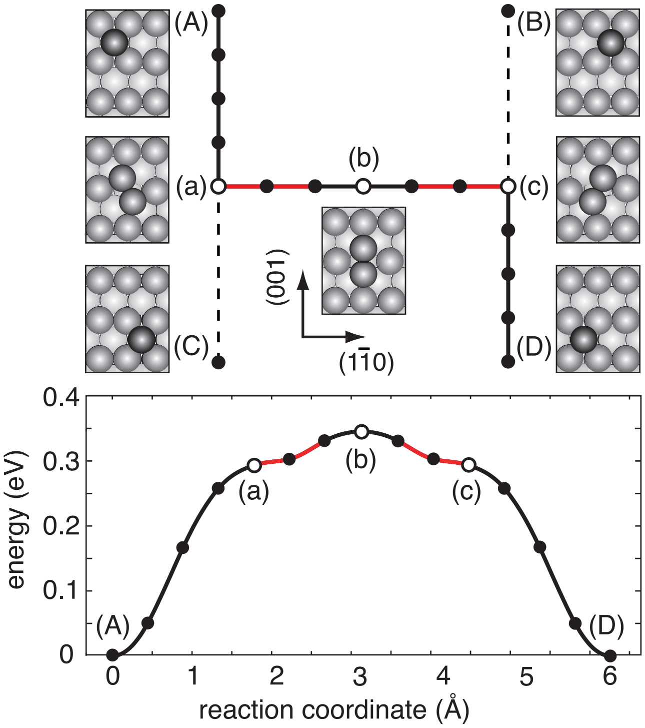

Figure 3.4: Al adatom cross-channel diffusion on Al(110) is shown between four minima (A)-(D). Saddles (a) and (c) correspond to diagonal exchange processes where the adatom pushes a surface row-atom into the neighboring channel along the $1\bar{1}1$ and $\bar{1}11$ directions, respectively. There is also a higher-energy cross-channel mechanism through saddle (b). The SD path found by an NEB through this saddle connecting minima (A) and (D) is shown to pass through the lower energy saddles (a) and (c) via the ridge segments, shown in red.

when the SD path approaches a saddle via a potential energy ridge.

3.5 Acknowledgements

We would like to thank Dr. Wolfgang Quapp and Antoni Aguilar-Mogas for supplying their Fortran codes and for helpful correspondence. This work was supported by the National Science Foundation grant number CHE-0645497 and the Texas Advanced Computing Center.

Chapter 4

Intrinsic Diffusion of Hydrogen on Rutile $TiO_2(110)$

4.1 Abstract

The theoretical part of a combined experimental and theoretical study of intrinsic hydrogen diffusion on bridge-bonded oxygen (BBO) rows of $TiO_2(110)$ is presented[41]. Sequences of isothermal scanning tunneling microscopy images demonstrate a complex behavior of hydrogen formed by water dissociation on BBO vacancies. Different diffusion rates are observed for the two hydrogens in the original geminate OH pair suggesting the presence of a long-lived polaronic state. For the case of separated hydroxyls, both theory and experiment yield comparable temperature-dependent diffusion rates. Density functional theory calculations show that there are two comparable low energy diffusion pathways for hydrogen motion along the BBO from one BBO to its neighbor, one by a direct hop and the other by an intermediate minimum at a terrace O. The values of kinetic parameters (prefactors and diffusion barriers) determined experimentally and theoretically are significantly different and indicate the presence of a more complex diffusion mechanism. We speculate that the hydrogen diffusion proceeds via a two-step mechanism: the initial diffusion of localized charge, followed by the diffusion of hydrogen. Both experiment and

theory show the presence of repulsive OH-OH interactions.

4.2 Introduction

Due to its intriguing chemical and physical properties, TiO_2 has been widely investigated as a model metal oxide in both fundamental science and technological applications. Commercially, TiO_2 is used in numerous applications, such as solar cells, toxic materials conversion, air purifying, self-cleaning windows, etc[42, 43, 44]. TiO_2 is also considered a promising photocatalyst for water splitting and hydrogen production[44, 45, 46]. In surface science, rutile $TiO_2(110)$ has become the most studied oxide surface, and it is generally used to model the TiO_2 catalytic properties under ultrahigh vacuum (UHV) conditions[46, 47, 48, 49, 50, 51]. Partially reduced TiO_2 also provides an excellent prospect for imaging chemical reactions with atomic resolution using scanning tunneling microscopy (STM)[47, 52, 53, 54, 55]. Despite the fact that the understanding of TiO_2 chemistry has progressed significantly, further studies are required to fully elucidate the structure-activity relationships on this catalyst.

It has been shown that the surface defects play an important role in the chemistry of TiO_2[56, 57]. For the reduced rutile $TiO_2(110)$-1×1 surface, the bridge-bonded oxygen (BBO) vacancies (BBO_V's) are the most common point defects, and as such, they have been extensively studied[46, 48, 49, 54, 56, 57, 53, 55, 58, 59, 60]. For example, BBO_V's readily dissociate water yielding geminate pairs of OH groups on the same BBO row[55, 56, 57, 53]. Interestingly, a number of intriguing phenomena have been reported for what may appear as a relatively simple system. It has been shown that mobile Ti^{4+}-bound water molecules efficiently assist crossrow diffusion of the OH hydrogen[58, 61]. Our recent study revealed that the two OH groups in the geminate OH pair are not equivalent as evidenced by the difference in the intrinsic hydrogen diffusion rates along the BBO rows at 300 K [59].

Isothermal variable temperature STM was used to investigate the intrinsic hydrogen diffusion along the BBO rows. The experiment shows that inequivalence of two hydrogens to perform the first hop away from the geminate hydroxyl pair decreases with increasing temperature and hopping rates are found to be dependent on the hydroxyl-hydroxyl separation distance. The experimental prefactors are found to be significantly lower ($\sim 10^7$ s^{-1}) than we have calculated for the diffusion of hydrogen on a BBO row ($\sim 10^{12}$ s^{-1}). A two-step diffusion process consisting of the initial diffusion of charge and subsequent diffusion of hydrogen is postulated to explain this observation. Slightly lower hopping rates and a higher diffusion barrier are observed for deuterated water and are explained by a lower zero-point energy of deuterium as compared to hydrogen.

4.3 Computational Details

Density functional theory (DFT) was used to calculate the energetics of hydrogen diffusion along the BBO rows. All calculations were done using the plane-wave based Vienna Ab initio Simulation Package (VASP)[62]. Electron

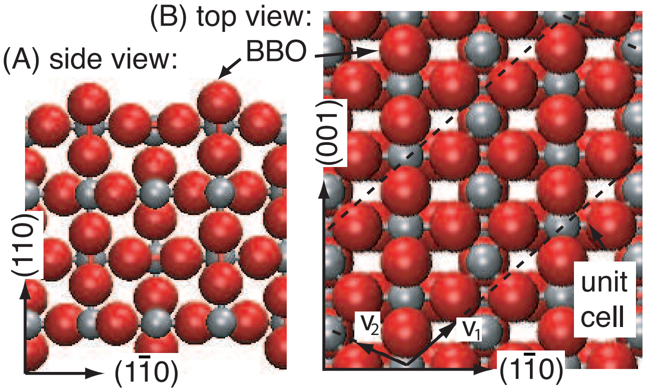

Figure 4.1: Unit cell from the side (A) along the BBO rows and top (B) showing the lattice vectors. O atoms are red; Ti are gray.

exchange and correlation were modeled with the PW91 generalized gradient approximation (GGA) functional[28]. Ultrasoft pseudopotentials of the Vanderbilt form[29] were used to describe core-valence interactions in the atomic core regions. Here, the valence electrons were kept orthogonal to a frozen core within the projector augmented wave (PAW) framework[30]. A 274 eV cutoff energy for the plane-wave basis set was found to be sufficient for the pseudopotentials used. The use of harder pseudopotentials for both hydrogen and oxygen with an energy cutoff of 400 eV results in a change of only 1% in the binding energy of hydrogen to the BBO row. A nonorthogonal unit cell (see Fig 4.1) was chosen to provide a long BBO row (six O atoms) and maximize the distance between periodic reactive sites. Tests showed that hydrogen binding energies were similar for slabs with four and five TiO_2 trilayers. A $1 \times 2 \times 1$ Monkhorst-Pack k-point mesh[31] was used to sample the Brillouin zone for the cell shown in Fig 4.1

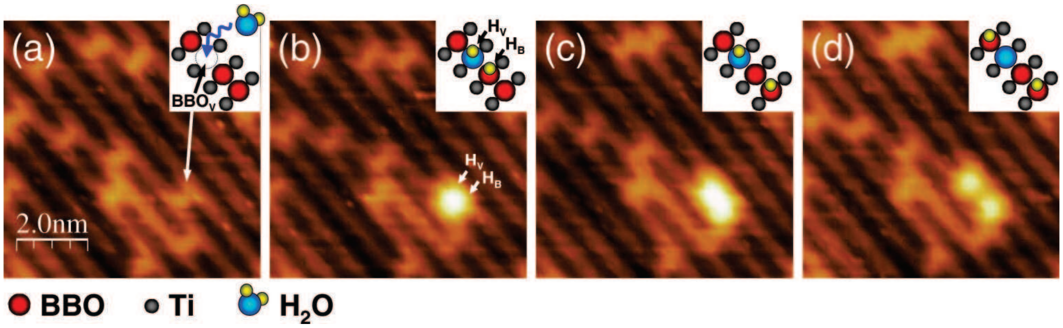

Figure 4.2: STM images of the same area on TiO_2 (110): (a) clean TiO_2(110) with bridge-bonded oxygen (BBO) vacancies (BBO$_V$s); (b) TiO_2(110) with a geminate hydroxyl pair formed by adsorption and dissociation of a water molecule. H_V marks the OH hydrogen, H_B marks the hydrogen that split off from the OH; (c) same area after a single hop of H_B hydrogen; and (d) after subsequent hop of H_V hydrogen. Insets exhibit the ball models illustrating the corresponding processes.

4.4 Results and Discussion

4.4.1 Hydrogen Diffusion from Geminate Hydroxyl Pairs.

Fig. 4.2 displays a sequence of images from an STM movie obtained at 357 K on the same area of initially clean TiO_2(110) (a), immediately after adsorption and dissociation of a single water molecule [53, 55, 58] (b) followed by the along-row diffusion of hydrogen atoms[58] (c and d). Since the empty state imaging of TiO_2(110) is dominated by electronic effects, the STM images show the reverse contrast of the real topography; i.e., the bright rows represent the topographically low lying Ti^{4+} rows, while the dark rows represent the topographically high BBO rows.[46] The bright protrusions on the dark rows are the BBO$_V$'s. The hydroxyl groups derived from the H_2O dissociation at BBO$_V$'s also appear as protrusions on the dark BBO rows, as shown in

Fig. 4.2. The brightness of the hydroxyl groups is generally higher than that of $\mathrm{BBO_V}$'s, but at lower imaging bias (<1 V) they can appear similar to $\mathrm{BBO_V}$'s. Great care by the experimentalist has been taken not to confuse these two features[59, 60].

In agreement with previous studies, we have observed that water dissociation at $\mathrm{BBO_V}$'s results in the formation of a geminate OH-OH pair as shown in Fig. 4.2b[53, 55, 58]. It is important to realize that the two OH groups in the pair are not created equally. The first one ($\mathrm{H_V}$) contains OH from the dissociated water molecule (O from H_2O is shown blue in the schematic), and the second one contains hydrogeonated from H_2O to a neighboring BBO ($\mathrm{H_B}$). Diffusion experiments show that the first hop, leading to the split of the geminate pair, is predominately (88%) performed by the $\mathrm{H_B}$ over $\mathrm{H_V}$ hydrogen as shown in Figure 4.2c. However, once the geminate pairs split apart, there is no measurable difference between the $\mathrm{H_B}$ and $\mathrm{H_V}$ hopping rates.

If first order kinetics are assumed experimental rates can be fit to the Arrhenius form

$$h_i = \nu_i e^{-E_i/k_\mathrm{B}T} \tag{4.1}$$

where the ν_B, E_B and ν_V, E_V are the prefactors and activation barriers for $\mathrm{H_B}$ and $\mathrm{H_V}$, respectively. The kinetic parameters for both the $\mathrm{H_B}$ and $\mathrm{H_V}$ hoping rates are determined to be

$$\begin{aligned} h_\mathrm{B} &= 2.0 \times 10^3 \mathrm{s}^{-1} e^{-0.42\mathrm{eV}/k_\mathrm{B}T} \\ h_\mathrm{V} &= 1.4 \times 10^6 \mathrm{s}^{-1} e^{-0.64\mathrm{eV}/k_\mathrm{B}T} \end{aligned} \tag{4.2}$$

Significant differences in the values of ν and ΔE for H_B and H_V clearly indicate the different characteristics of H_B and H_V hydrogen atoms in the geminate hydroxyl pairs. Furthermore, the low values of ν suggest that the nature of hydrogen diffusion from the geminate OH pair is complex. In a previous study[59], it is argued that the difference between H_B and H_V possibly originates from the different local environment experienced by H_B and H_V. While H_V has formally two Ti^{3+} ions underneath, H_B has only one. This simplistic picture assumes that charge distribution remains asymmetric on the time scale of minutes required to execute our experiments. One possible mechanism to stabilize such an asymmetric configuration is via formation of a long-lived polaronic state. We do not see such a state in our DFT calculations; the charge density is symmetric on H_B and H_V. This is likely due to the tendency for pure DFT (here, using the PW91 functional) to artificially delocalize electronic states. Interestingly, a recent theoretical study using DFT with a hybrid exchange-correlation functional (mixing a pure DFT functional with some portion of exact exchange) suggested that the excess charge associated with the vacancy is localized and asymmetrically distributed around the BBO_V[63]. Analogous results have also been observed for the BBO_V filled with a single OH[64]. We speculate that the conversion of such a polaronic state into a pair of two identical, decoupled OH groups may explain the complex kinetics observed for H_B and H_V diffusion. Further theoretical studies are required to address this issue.

4.4.2 Average Hydrogen Hopping Rates for Separated OH Species

To further explore the intrinsic diffusion of hydrogen we have determined the hopping rates after the separation of the geminate OH pairs. The experiments yield prefactors, ν, of $10^{7.3\pm0.4}$ and $10^{8.6\pm0.6}$ s^{-1} and activation barriers, E, of 0.74 ± 0.03 eV and 0.85 ± 0.04 eV for the dosed H_2O and D_2O, respectively. The ν and E values for background dosed H_2O of $10^{7.6\pm0.6}$ s^{-1} and 0.76 ± 0.06 eV are, within the error limits, identical to the values for dosed H_2O. Analogous to the low ν values measured in the previous section for the H_B and H_V hops, the values of ν measured for separated hydrogens are also too low to correspond to a simple one-step, purely thermally driven diffusion process. We have considered tunneling as a possible reason for the low ν and E values, but the similar behavior for hydrogen and deuterium strongly suggests that tunneling is not a dominant factor controlling the diffusion process. The fact that the diffusion barrier for D is slightly higher is most likely the result of a lower zero-point energy for the heavier isotope. DFT calculations of the zero-point energy predict a 0.04 eV higher diffusion barrier for D than for H. This is smaller but on the same order as the experimentally observed isotope shift.

DFT calculations were used to explore the mechanism and rate of H hopping along the BBO row. To do this, an H atom was placed on a BBO site in the unit cell illustrated in Figure 4.1 and minimized to generate an initial state. The H was then moved to an adjacent BBO site and minimized into a final state. A nudged elastic band (NEB) was then relaxed between these

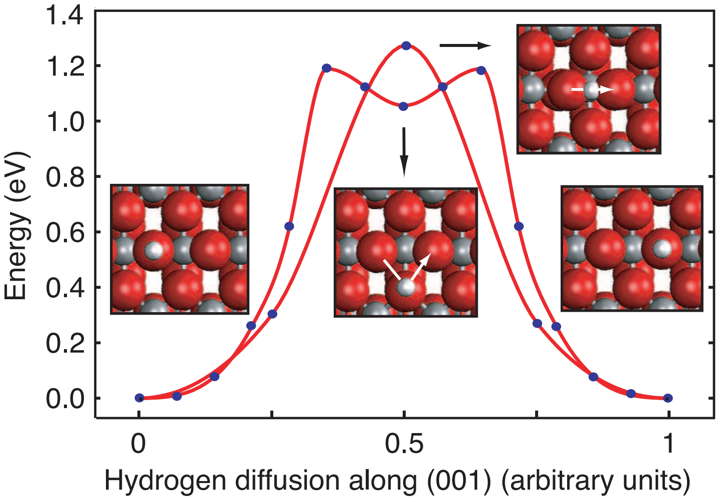

Figure 4.3: H diffuses along the BBO row via two mechanisms: direct hop with a barrier of 1.29 eV, and through a relay-point intermediate minimum (1.07 eV) with a barrier of 1.19 eV. Ti atoms are gray, O atoms are red, and the diffusing H atom is white.

states to find a minimum energy pathway. The climbing image NEB method was used to rigorously converge upon the saddle point and accurately calculate the activation energy. The H atom was found to hop directly along the BBO row, dipping into a saddle point between adjacent BBO atoms (see Figure 4.3). The activation energy for this process is 1.29 eV. We also investigated a mechanism reported in a recent study, in which H diffuses along the BBO row via a relay-point O atom on the terrace, adjacent to the BBO row[65]. This study reports the relay point to be a saddle with an energy of 0.87 eV. Here, we find that the relay point is a shallow local minimum with an energy of 1.07 eV and that a barrier of 1.19 eV is required for the H to diffuse into it. There are differences between these calculations that can account for the variation in energetics, including the functional, polarization correction, and the method of determining the reaction pathways. Figure 4.3 shows the energy profiles for both diffusion mechanisms. Since the two mechanisms have comparable barriers, the overall rate has been calculated as the sum of the direct hop process and the two equivalent relay-point processes.

Prefactors for the H diffusion mechanisms were calculated by displacing all non-frozen atoms by a finite difference step of 0.001 Å, building a Hessian matrix from the difference in forces, and diagonalizing it to find the harmonic modes at the minima and saddle point. We find standard prefactors for the elementary reactions of 3.5×10^{12} s^{-1} (direct hop) and 5.9×10^{11} s^{-1} (relay-point), with an effective overall prefactor of 4.1×10^{12} s^{-1}. Here, a dynamical correction factor of 0.5 is included for the relay-point mechanism, because we are assuming that it is equally likely to hop back to the initial state as to the final state from the relay-point minimum. Although we calculate a standard prefactor, it is five orders of magnitude larger than the prefactor determined from experiment.

Figure 4.4 is an Arrhenius plot showing the rate of H hopping along the BBO row. The dashed line is the sum of the classical harmonic transition state theory rates (see Eq. 4.1) for the relevant processes, based upon the DFT barrier and prefactor. It is remarkable that the calculated rate is very similar to the experimental rate in the temperature range of the experiments, even though the barrier and prefactor are individually found to be very different.

One possibility is that the low experimental barrier and prefactor are

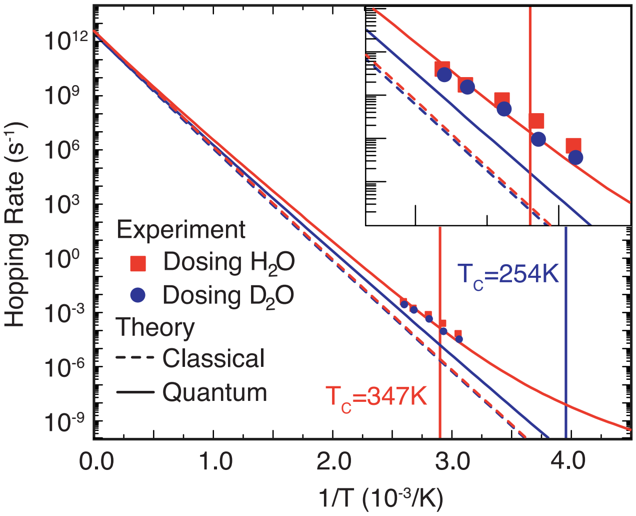

Figure 4.4: Arrhenius plot of H (red) and D (blue) diffusion along the BBO row. The dashed line shows the hoping rate calculated from classical harmonic transition state theory with rate contributions from the direct hop and relay-point pathways. The solid line shows the rate corrected by both zero-point energy (based upon replacing the classical harmonic partition function with the quantum one) and a tunneling correction (based upon approximating the barrier as a symmetric Eckart potential for the direct hop process). The crossover temperature for hydrogen diffusion, $T_c = 347$ K, is where the harmonic tunneling correction diverge, and where tunneling contributes significantly to the rate. There is a smaller quantum tunneling effect for D diffusion and a lower crossover temperature of 245 K.

due to quantum effects. To investigate this, we have applied a quantum correction to our calculated rate (solid line). A zero-point energy correction was calculated for all positive modes at the minima and saddle from the ratio of the quantum to classical harmonic partition functions[66, 67]. A tunneling correction was also applied by approximating the barrier as a symmetric Eckart potential, for which there is an analytic form of this correction[68]. The tem-

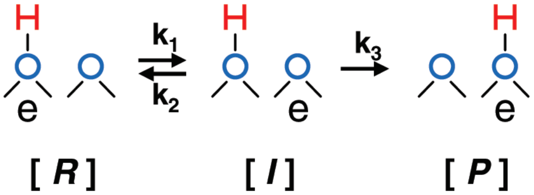

Figure 4.5: Proposed model with two-step mechanism for along-row hydrogen-charge pair (labeled R) diffusion on BBO rows of $TiO_2(110)$. The initial step, the diffusion of charge, leads to a separated hydrogen-charge pair intermediate. The rate of formation of I from R is determined by the rate constant, k_1. The pathway to reformation of R will proceed via charge migration back to the reactant basin with rate constant, k_2. The process competing with the reformation of reactant via k_2 is the migration of hydrogen to create the coupled hydrogen-charge pair, P, in location displaced by one BBO atom.

perature below which tunneling becomes important can be calculated from the crossover temperature, $T_c = \eta|\nu^*|/k\text{B}$, where ν^* is the imaginary frequency along the negative curvature mode at the saddle point. The contribution from tunneling is only significant for the direct hop process; the relay-point process has a much broader barrier and a low crossover temperature. Figure 4.4 shows the quantum rate for hydrogen diffusion (solid line) and the crossover temperature (vertical line). While it is encouraging that $T_c = 347$ K (direct hop) falls in the range of the experimental data, suggesting that tunneling is important for the diffusion process, it would not be fair to conclude that quantum corrections bring theory into better agreement with experiment or that they explain the anomalously low prefactor and barrier derived from experiment.

As already discussed, the diffusion barriers for both direct and relay pathways are significantly higher than the barrier observed in our experiments. To explain the low values of ν and E found in our experiment, we propose a two-step diffusion mechanism as schematically shown in Figure 4.5. Prior spectroscopic evidence points to the fact that the band gap defect states observed on $TiO_2(110)$ are related to surface defects which are most likely BBO_Vs[46, 57, 69, 70]. In particular, the electron energy loss spectroscopy (EELS) study[57] clearly shows that these states are preserved upon H_2O adsorption and dissociation at BBO_Vs but are completely annihilated upon O_2 adsorption and dissociation. It is plausible to assume that the extra charge density associated with these states remains spatially correlated with the hydroxyl groups as they diffuse along the surface. Such a correlated hydrogen-charge pair is schematically shown as the reactant, R, on the left side of the schematic shown in Figure 4.5. In our model we propose sequential diffusion of charge followed by hydrogen. Assuming that the correlated hydrogen-charge pair is the low energy configuration, decoupling the charge from the hydrogen leads to the formation of metastable, decoupled hydrogen-charge intermediate, I. The rate of formation of I from R is determined by the rate constant k_1. The pathway to reform the original coupled hydrogen-charge pair will proceed via charge migration back to the reactant basin with the rate constant k_2. The process competing with the reformation of reactant via k_2 is the migration of hydrogen to create the coupled hydrogen-charge pair, P, in a location displaced by one lattice space along the BBO row as shown on the right side of Figure 4.5. This step may involve a direct H hop from one BBO atom to its neighbor or a two-step H motion via relay mechanism as suggested by the theoretical calculation (see Figure 4.3). It is reasonable to assume that the hydrogen diffusion rate (rate constant k_3) will be significantly smaller than that for the charge migration back to the original position (rate constant k_2). The rate equations describing the reaction scheme in Figure **??** are summarized below:

$$\begin{aligned} [\dot{\mathrm{R}}] &= -k_1[\mathrm{R}] + k_2[\mathrm{I}] \\ [\dot{\mathrm{I}}] &= -k_2[\mathrm{I}] + k_3[\mathrm{I}] \\ [\dot{\mathrm{P}}] &= k_3[\mathrm{I}] \end{aligned} \tag{4.3}$$

Under the steady state approximation, $[\dot{\mathrm{I}}] = 0$, we obtain the rate of reactant consumption as follows:

$$[\dot{\mathrm{R}}] = -\frac{k_1 k_3}{k_2 + k_3}[\mathrm{R}] \tag{4.4}$$

Assuming Arrhenius forms for all the rate constants, k_1, k_2, and k_3, and $k_3 \ll k_2$ we obtain the final expression for the rate of reactant consumption, $[\dot{\mathrm{R}}]$, in our model as follows:

$$[\dot{\mathrm{R}}] \approx -\frac{\nu_1 \nu_3}{\nu_2} \exp(-\frac{E_1 + E_3 - E_2}{RT})[\mathrm{R}] \tag{4.5}$$

A reasonable range of individual prefactors, ν_1, ν_2, and ν_3, within $10^{11} - 10^{15}$ s^{-1} yields the range of observable prefactors, $\nu_{\mathrm{eff}} = \nu_1 \nu_3 / \nu_2$, between 10^7 and 10^{19} s^{-1}. The low limit value of 10^7 s^{-1} is of the same order of magnitude as the value of $10^{7.3}$ s^{-1} determined in the experiments.

Further theoretical studies employing state-of-the-art techniques such as hybrid DFT[63] and DFT+U[71] are required to provide a deeper understanding of the underlying diffusion mechanism of hydrogen on $\mathrm{TiO_2}(110)$.

These methods show localized electronic states at vacancies on the BBO rows, which are expected to persist upon H_2O adsorption. A localized electronic state could validate our two-step rate model or show other changes to the DFT energetics that result in the low hydrogen diffusion prefactor and barrier observed in our experiments.

4.4.3 Hydrogen-Hydrogen Separation Dependent Hopping Rates

Experimentally separation-dependent diffusion barriers increase monotonically from 0.73 ± 0.003 to 0.77 ± 0.007 eV as the separation distance increases from 2 to 6 lattice spaces. It should be emphasized that these values are significantly larger than the diffusion barriers determined for H (0.42 eV) and H_V (0.64 eV) for the separation of the geminate hydroxyl pair. Forward hops were found to be preferred at all temperatures: for separation 2 sites by a factor of 2.6 ± 0.3, for 3 sites by 1.4 ± 0.2, and for 4 sites by 1.0 ± 0.2. In addition decreasing hopping rates and the increasing diffusion barriers with increasing separation indicate that the OH-OH interactions are repulsive and that the ground state of the isolated OH is lower than that of the OH in the proximity of another OH.

The theoretically determined energy landscape for H_2O dissociation and the subsequent diffusion of H_B away from H_V along the BBO row is summarized in Figure 4.6. The barrier for dissociation of H_2O into separated OH groups is only 0.31 eV, so that this process is expected to occur spontaneously on the time scale of the experiments. The H hopping barrier is found to be

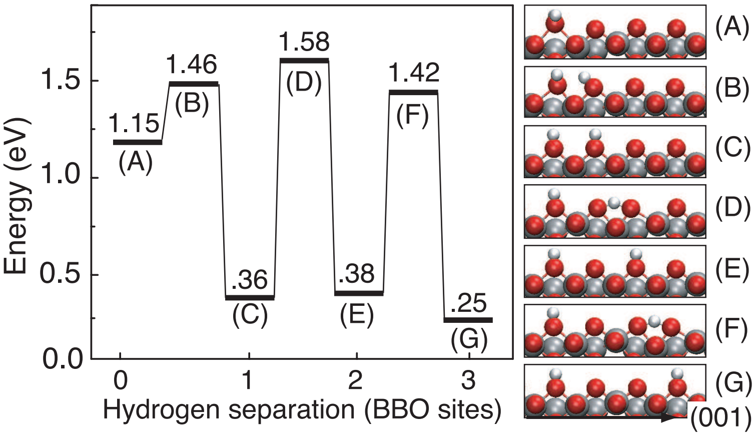

Figure 4.6: Theoretically determined energy landscape for the dissociation of water in a BBO_V site (A-C), and the subsequent diffusion of a hydrogen atom along the BBO row (C-G). The zero of energy corresponds to separated H atoms on BBO sites.

somewhat higher for the first hop (1.22 eV), taking the H atoms from adjacent BBO sites to those separated by one BBO, then for the next hop (1.04 eV), in which the H atoms end up separated by two BBO sites. The interaction energy between the H atoms is found to be repulsive, as is found in the experiment, in part due to dipole-dipole interactions. A Bader charge analysis was used to estimate this interaction[72, 73]. A charge of 0.64 e^- was found to transfer from the adsorbed H to the BBO row, resulting in a 0.21 eV dipole-dipole repulsion between H atoms adsorbed on adjacent BBO sites. It should be noted that the uncertainties in the DFT energetics (> 0.1 eV) are significantly larger than the change in hopping barriers found in the experiment (0.04 eV).

4.5 Summary

This is the theoretical portion of a combined experimental and theoretical investigation of the intrinsic hydrogen diffusion along the BBO rows of the $TiO_2(110)$ surface. Significantly different diffusion rates are observed for the two hydrogens in the original geminate OH pair during the split. We speculate that this inequivalence of the two OH groups is indicative of the presence of a long-lived polaronic state which is not reproduced in our DFT calculations. For the case of separated hydroxyls, both theory and experiment yield comparable temperature-dependent diffusion rates. Density functional theory calculations show that there are two comparable low energy diffusion pathways for hydrogen motion along the BBO from one BBO to its neighbor, one by a direct hop and the other by an intermediate minimum at a terrace O. The values of kinetic parameters, prefactors, and diffusion barriers, determined experimentally and theoretically, are significantly different and point to a more complex diffusion mechanism. Our interpretation invokes the two-step mechanism with the initial diffusion of localized charge followed by the diffusion of hydrogen along the BBO row. Both experiment and theory show the presence of repulsive OH-OH interactions. The surprisingly complex and intriguing behavior of hydrogen on $TiO_2(110)$ points to our limited understanding of this model oxide surface.

4.6 Acknowledgments

This work was supported by the U.S. Department of Energy's Office of Basic Energy Sciences, Chemical Sciences Division, Robert A. Welch Foundation, and National Science Foundation (CHE-0412609 and CHE-0645497) and performed at W. R. Wiley Environmental Molecular Science Laboratory, a national scientific user facility sponsored by the Department of Energys Office of Biological and Environmental Research located at Pacific Northwest National Laboratory (PNNL). PNNL is operated for the U.S. DOE by Battelle under Contract No. DEAC06-76RLO 1830.

Chapter 5

Alchemical Derivatives of Reaction Energetics

5.1 Abstract

Based on molecular grand canonical ensemble density functional theory, we present a theoretical description of how reaction barriers and enthalpies change as atoms in the system are subjected to alchemical transformations, from one element into another. The change in the energy barrier for the umbrella inversion of ammonia is calculated along an alchemical path in which the molecule is transformed into water, and the change in the enthalpy of protonation for methane is calculated as the molecule is transformed into a neon atom *via* ammonia, water, and hydrogen fluoride. Alchemical derivatives are calculated analytically from the electrostatic potential in the unperturbed system, and compared to numerical derivatives calculated with finite difference interpolation of the pseudopotentials for the atoms being transformed. Good agreement is found between the analytical and numerical derivatives. Alchemical derivatives are also shown to be predictive for integer changes in atomic numbers for oxygen binding to a 79-atom palladium nanoparticle, illustrating their potential use in gradient-based optimization algorithms for the rational design of catalysts.

Table 5.1: Investigated properties, reaction enthalpies ΔH and energy barriers E^{act}, and chemical species connected by alchemical paths *via* the order parameter λ. ($0 \leq \lambda \leq 1$)

λ=0	λ=1	property
CH_4	NH_3	ΔH
NH_3	H_2O	ΔH, E^{act}
H_2O	HF	ΔH
HF	Ne	ΔH

5.2 Introduction

Chemical compound space (CCS) can be defined as the set of all combinations of chemical elements in all geometric isomers. Combinatorial exploration of CCS has been used to produce large virtual chemical databases [74, 75] which would then need to be searched to find the compound with the property of interest [76, 77, 78]. More efficient approaches to search CCS include simulated annealing [79], genetic algorithms [80], cluster expansions that can be combined with density functional theory [81], optimizations based on alchemical gradients [82, 83, 84, 85], or various optimization methods in the coefficient space of linear combinations of atomic potentials [86, 87, 88, 89, 90, 91].

The energetics of chemical reactions that involve geometrical changes are relevant for many important phenomena. In this study, we address the effect of varying stoichiometry on properties which are explicitly geometry dependent, such as activation barriers or reaction enthalpies.

First, we have studied the effect of alchemical transformation for simple molecular model systems, for which we can easily assess accuracy and demonstrate numerical feasibility. In particular, we choose a subset of CCS including only stable compounds containing 10 protons and electrons, such as CH_4, where a central atom is saturated with hydrogens. Table 5.2 shows the alchemical paths and properties which have been investigated. Reaction protonation enthalpies along the four continuous transformations, $CH_4 \rightarrow NH_3 \rightarrow H_2O \rightarrow HF \rightarrow Ne$, have been computed, as well as the activation energy for the umbrella flipping of ammonia as it is continuously transformed into a water molecule. Analytical alchemical derivatives along each stoichiometrical transformation were calculated and compared to their finite difference analogue.

Secondly, we examine alchemical derivatives for the binding energy of oxygen to a nanoparticle. It has been shown by Nørskov and coworkers [92] that the binding energy of oxygen to a metal surface can be used to predict its catalytic activity for the oxygen reduction reaction. This reaction is important because it limits the kinetics in fuel cell cathodes. We show how alchemical derivatives can be used to navigate the CCS of nanoparticles to tune the oxygen binding energy.

In these examples, we show how analytic alchemical derivatives, which can be evaluated from single point energy calculations, are consistent with finite difference derivatives calculated from interpolation of the pseudopotentials. We also show how well the analytic derivatives work for predicting changes in binding energies and barriers over integer changes in atomic numbers. This is particularly important for the use of alchemical derivatives in gradient based optimization of material properties.

5.3 Theory

5.3.1 Taylor Expansion in Chemical Space

Free energy differences can be evaluated between any two distinct thermodynamic states through thermodynamic integration [93, 94], and variants of it, such as free energy perturbation methods [95]. Typically, an order parameter, λ, is used to drive the system from one state to the other. Integration over the statistical mechanical ensemble averages of the force over λ yields the free energy difference between the two states. In the same way, we use here λ to express a compound's potential energy as a Taylor expansion in CCS around a reference compound, where $\lambda = 0$ and the energy is E^0. The energy of any other compound, for which $\lambda = 1$, is approximated as

$$E(\lambda = 1) = E^0 + \partial_\lambda E^0 \ \Delta\lambda + \frac{1}{2}\partial_\lambda^2 E^0 \ \Delta\lambda^2 + \mathrm{HOT} \tag{5.1}$$

where $\Delta\lambda = 1$, $\partial_\lambda E$ denotes the derivative of E with respect to λ and HOT are the higher order terms.

Within density functional theory (DFT) [96], a compound is defined by its proton density distribution, $Z(\mathbf{r})$, and the number of electrons N_e which—after the self-consistent field cycle—yield the ground state electron density, ρ. These quantities constitute the extensive particle variables within molecular grand canonical DFT [83]. Since we explicitly focus on compounds with different geometries it is now convenient to include the positions of the nuclei $\{\mathbf{R}_I\}$ in the set of extensive variables, assuming the conventional classical point charge distribution of atomic numbers, $Z(\mathbf{r}) = \sum_I N_I \delta(\mathbf{R}_I - \mathbf{r})$, where N_I is the atomic number of atom I.

Consequently, the first order term from Eq. (5.1) is

$$\begin{aligned}\partial_\lambda E &= \int d\mathbf{r}\; \delta_{Z(\mathbf{r})}E\; \partial_\lambda Z(\mathbf{r}) + \sum_I \partial_{\mathbf{R}_I} E \cdot \partial_\lambda \mathbf{R}_I \\ &\quad + \partial_{N_e} E\; \partial_\lambda N_e \\ &= \int d\mathbf{r}\; \mu_n(\mathbf{r})\; \partial_\lambda Z(\mathbf{r}) - \sum_I \mathbf{F}_I \cdot \partial_\lambda \mathbf{R}_I \\ &\quad + \mu_e\; \partial_\lambda N_e. \end{aligned} \tag{5.2}$$

The nuclear chemical potential, $\delta_{Z(\mathbf{r})}E = \mu_n(\mathbf{r})$, is the derivative of the energy with respect to variation in the nuclear charge distribution. At the position of atom I, $\mu_n(\mathbf{R}_I)$ is the derivative of the energy with respect to the nuclear charge $Z(\mathbf{R}_I)$. It is therefore called the "alchemical potential." The ionic forces, $\{\mathbf{F}_I\}$, are the negative gradients of the energy with respect to atomic position. The electronic chemical potential μ_e is the derivative of the energy with respect to a change in N_e, i.e. the molecular eigenvalue of the highest occupied molecular Kohn-Sham orbital [97, 98].

Analogously, the second order term from Eq. (5.1) can be obtained, and contains all the pure and mixed second order derivatives such as: the alchemical hardness $\delta_{Z(\mathbf{r})}\delta_{Z(\mathbf{r}')}E = \delta_{Z(\mathbf{r}')}\mu_n(\mathbf{r}) = \eta_n(\mathbf{r},\mathbf{r}')$; the electronic hardness, $\partial_{N_e}\partial_{N_e}E = \partial_{N_e}\mu_e = \eta_e$; and the Hessian matrix, $\partial_{\mathbf{R}_I}\partial_{\mathbf{R}_J}E = \partial_{\mathbf{R}_J}\mathbf{F}_I = \kappa_{IJ}$; the "force Fukui" function $\delta_{Z(\mathbf{r})}\partial_{\mathbf{R}_I}E = -\delta_{Z(\mathbf{r})}\mathbf{F}_I = \partial_{\mathbf{R}_I}\mu_n(\mathbf{r}) = \mathit{ff}(\mathbf{R}_I,\mathbf{r})$; the molecular Fukui function $\partial_{N_e}\delta_{Z(\mathbf{r})}E = \partial_{N_e}\mu_n(\mathbf{r}) = \delta_{Z(\mathbf{r})}\mu_e = f_m(\mathbf{r})$; and the nuclear Fukui function $\partial_{N_e}\partial_{\mathbf{R}_I}E = -\partial_{N_e}\mathbf{F}_I = \partial_{\mathbf{R}_I}\mu_e = f_n(\mathbf{R}_I)$.

The (arbitrary) path along λ can be chosen to simplify the number of terms in Eq. (5.2). For the small molecules in the first part of this study, we have chosen to relax the geometry of the molecule along λ so that $E(\lambda)$ is minimal with respect to geometrical variation, and the term containing $\mathbf{F}$ vanishes. Furthermore, we restrict ourselves to alchemical transformations with a constant N_e equal to 8 valence electrons (iso-electronic). For such paths Eq. (5.2) reduces to

$$\partial_\lambda E = \int d\mathbf{r}\ \mu_n(\mathbf{r})\ \partial_\lambda Z(\mathbf{r}). \tag{5.3}$$

The alchemical derivative of Eq. (5.3) describes the change in energy along the path λ as the integral over the change in proton density, $Z(\mathbf{r})$, times the nuclear chemical potential, $\mu_n(\mathbf{r})$.

5.3.2 Alchemical Derivatives

The nuclear chemical potential, $\mu_n(\mathbf{r})$, was derived in Ref. [83] as an electrostatic potential,

$$\mu_n(\mathbf{r}) = \int d\mathbf{r}' \frac{Z(\mathbf{r}')\,\mathrm{erf}(\sigma|\mathbf{r}-\mathbf{r}'|) - \rho(\mathbf{r}')}{|\mathbf{r}-\mathbf{r}'|} \tag{5.4}$$

modified with an error function to switch off intra-nuclear interactions. This switching function is required for any $\mathbf{r}$ for which $Z(\mathbf{r}) > 0$, i.e. at an atomic center $\mathbf{R}_I$. At this point, proton density would be added to an existing nucleus, diverging the electrostatic interaction. In principle, choosing a small value of σ will eliminate such divergences from the integral. In practice, the nuclear charge at $\mathbf{R}_I$ is simply excluded from the evaluation of $\mu_n(\mathbf{R}_I)$.

Changing the proton density at the nuclei is of particular interest because this changes an atom from one element to another. The corresponding molecular nuclear alchemical derivative can be defined as the sum over the product of alchemical potentials with changes in atomic number,

$$\partial_\lambda E = \sum_I \mu_n(\mathbf{R}_I)\ \partial_\lambda N_I. \tag{5.5}$$

The focus of this work is to calculate the alchemical derivative of an energy difference, $\Delta E = E^b - E^a$, between two molecular geometries $\{\mathbf{R}_I^a\}$ and $\{\mathbf{R}_I^b\}$. This can be written in terms of a difference in the nuclear chemical potential,

$$\partial_\lambda \Delta E = \int d\mathbf{r}\ \Delta\mu_n(\mathbf{r})\ \partial_\lambda Z(\mathbf{r}), \tag{5.6}$$

where $\Delta\mu_n(\mathbf{r}) = \mu_n^b(\mathbf{r}) - \mu_n^a(\mathbf{r})$. In the special case that all nuclei have the same position in molecules a and b, so $\{\mathbf{R}_I^a\} = \{\mathbf{R}_I^b\} = \{\mathbf{R}_I\}$, the alchemical potential difference reduces according to Eq. 5.4 to

$$\begin{aligned} \Delta\mu_n(\mathbf{R}_I) &= \mu_n^b(\mathbf{R}_I) - \mu_n^a(\mathbf{R}_I) \\ &= -\int d\mathbf{r} \frac{\rho^b(\mathbf{r}) - \rho^a(\mathbf{r})}{|\mathbf{R}_I - \mathbf{r}|} \end{aligned} \tag{5.7}$$

where $\rho^a(\mathbf{r})$ and $\rho^b(\mathbf{r})$ are the electronic charge densities in molecules a and b respectively.

5.3.3 Varying Molecular Geometries

Here we are interested in energy differences between molecules with different geometries, where $\{\mathbf{R}_I^a\} \neq \{\mathbf{R}_I^b\}$. When the position of nucleus I changes, the alchemical potential difference can no longer be defined at the position of the nucleus as $\Delta\mu_n(\mathbf{R}_I)$. Instead, we use the index of the nucleus,

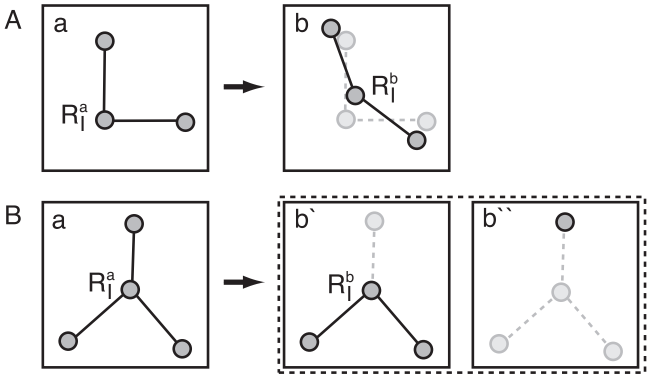

Figure 5.1: (A) Activation energies are calculated as the energy difference between two geometries; the corresponding alchemical derivative at atom I is defined in Eq. 5.9. (B) In a dissociation reaction where atom I is only present in the reactant and product space a and b', respectively, space b'' does not contribute to the alchemical derivative $\Delta\mu_{n,I}$.

I, to identify the alchemical potential difference,

$$\Delta\mu_{n,I} = \mu_n^b(\mathbf{R}_I^b) - \mu_n^a(\mathbf{R}_I^a), \tag{5.8}$$

and the derivative of the energy difference along λ is

$$\partial_\lambda \Delta E = \sum_I \Delta\mu_{n,I}\ \partial_\lambda N_I. \tag{5.9}$$

5.3.4 Activation and Protonation Energies

Two examples of reaction energetics involving molecules of different geometries are illustrated schematically in Fig. 5.1, an activation energy (A) and a protonation energy (B). The activation energy is the energy difference between two geometries, the initial state $\{\mathbf{R}_I^{\text{init}}\}$ and the transition state $\{\mathbf{R}_I^{\text{ts}}\}$,

$E^{\text{act}} = E^{\text{ts}} - E^{\text{init}}$. Its derivative along the path λ is

$$\partial_\lambda E^{\text{act}} = \sum_I \mu_{n,I}^{\text{act}}\, \partial_\lambda N_I, \tag{5.10}$$

where $\mu_{n,I}^{\text{act}} = \mu_n^{\text{ts}}(\mathbf{R}_I^{\text{ts}}) - \mu_n^{\text{init}}(\mathbf{R}_I^{\text{init}})$.

The reaction energy E^{rxn} and its alchemical potential at atom I, $\mu_{n,I}^{\text{rxn}}$, are defined in analogy, substituting the final state for the transition state. In this work, we chose the protonation of a molecule as the reaction energy to be calculated,

$$E^{\text{prot}} = E^{\text{mol+H}^+} - E^{\text{mol}} - E^{\text{H}^+}. \tag{5.11}$$

This is illustrated in Fig. 5.1(B) where a is the protonated molecule and b contains both the isolated molecule (b') and proton (b''). When the molecular geometry is relaxed, the alchemical derivatives at the atoms can be calculated using Eq. (5.8) and the derivative of E^{prot} along λ using Eq. (5.9). If the geometry of the molecule is held fixed, the alchemical potential is defined as

$$\begin{aligned}\mu_n^{\text{prot}}(\mathbf{r}) &= \delta_{Z(\mathbf{r})} E^{\text{prot}} \qquad (5.12)\\ &= \mu_n^{\text{mol+H}^+}(\mathbf{r}) - \mu_n^{\text{mol}}(\mathbf{r}) - \mu_n^{\text{H}^+}(\mathbf{r})\end{aligned}$$

Note that this expression describes the energy of adding proton density anywhere in space, not just at existing atoms. There is, however, a subtlety in Eq. (5.12) related to how reaction energies are calculated with DFT. The three terms in Eq. (5.11) are calculated separately as illustrated in Fig. 5.1(B). Even though the atoms are fixed in space, $\mu_n^{\text{mol}}(\mathbf{r})$ and $\mu_n^{\text{H}^+}(\mathbf{r})$ are calculated in different spaces b' and b''; they do not share the same coordinate, $\mathbf{r}$. To calculate an alchemical change in the energy one must decide in which space the change occurs, $\mathbf{r}^{\mathrm{mol}}$ or $\mathbf{r}^{\mathrm{H}^+}$. If the change is in $\mathbf{r}^{\mathrm{mol}}$ then $\mu_n^{\mathrm{H}^+}$ vanishes in Eq. (5.12).

5.3.5 Alchemical Derivatives via Finite Difference

Eq. (5.5) can be written as a finite difference derivative,

$$\frac{\Delta E}{\Delta \lambda} = \sum_I \frac{\Delta E}{\Delta N_I} \frac{\Delta N_I}{\Delta \lambda}. \tag{5.13}$$

Note here that ΔE is a change in energy with respect to λ and not a change with respect to geometry, as in Eq. (5.6). In standard electronic structure calculations the atomic numbers N_I are integers. The alchemical potential, $\Delta E / \Delta N_I$ could be evaluated with integer N_I, but we are interested in using a smaller (non-integer) finite difference step size in order to numerically verify the analytic derivative from Eq. (5.4). To this end we choose to represent an atom with a fractional atomic number by a pseudopotential that is linearly interpolated between the atoms of nearest integer atomic numbers. For example, an atom which is fractionally higher by an amount f than the atomic species with integer atomic number N, the pseudopotential is interpolated as

$$V_{N+f}^{PP} = (1-f)\, V_N^{PP} + f\, V_{N+1}^{PP}. \tag{5.14}$$

With interpolated pseudopotentials we can calculate both E and $\mu_{n,I}$ at any non-integer value of N_I and thus the finite difference derivatives for any value of λ along an alchemical transition. Energies were calculated along paths, $\lambda \in [0, 1]$, in increments of 0.1. Finite difference alchemical derivatives were taken at these points using central difference with a step size of $\Delta\lambda = 0.005$.

5.4 Computational Details

DFT [96, 99] calculations were performed using the generalized gradient approximated exchange-correlation potential PBE [100], as implemented in Vienna *ab initio* simulation package, VASP [101, 102]. Core electrons were represented using the projector augmented wave method [103, 104]; valence electrons with a plane wave basis set up to an energy cutoff of 400 eV. A cubic cell of dimension 10 Å was used for molecules and 20 Å for nanoparticles. Geometry relaxation was continued until the force dropped below 0.01 eV/Å for each atom. In VASP charged cells are with a uniform background counter-charge.

Analytical alchemical potentials were evaluated from Eq. (5.4) on a uniform grid with 20-30 points/Å using the electrostatic potential output. To reduce finite grid-based errors when taking differences such as in Eq. (5.8) the position of the atoms $\mathbf{R}_I^a$ and $\mathbf{R}_I^b$ were translated to the same position on the grid.

A calculation of $\partial_\lambda E$ requires a path of alchemical transformation $N_I(\lambda)$ connecting the initial and final atomic number N_I^a and N_I^b. We have chosen paths in which the N_I vary linearly in λ,

$$N_I(\lambda) = (1 - \lambda)\; N_I^a + \lambda\; N_I^b. \tag{5.15}$$

This choice is convenient because the derivative is a constant along the path,

$$\partial_\lambda N_I(\lambda) = \partial_\lambda N_I = N_I^b - N_I^a, \tag{5.16}$$

and depends only on the endpoints.

5.5 Results and Discussion

Two test cases are used to verify that the analytic alchemical derivatives are consistent with numerical finite difference derivatives of the pseudopotentials. First, the umbrella flipping of ammonia is used to test the change in activation energies. Then, second, the protonation of small molecules is used to test derivatives in reaction enthalpies for both frozen and relaxed geometries. In both cases, there is good agreement between the analytical and numerical alchemical derivatives. Finally, we show a more interesting example of oxygen binding to a palladium nanoparticle. Here, we test the predictive power of the alchemical derivatives for integer changes in the atomic number of the metal atoms in the nanoparticle, and show that the derivatives can be used to tune the binding energy of oxygen with respect to the particle composition.

5.5.1 Activation Energies

The energy barrier is a geometry dependent property where the configurations of the transition state and initial state differ and as such explicitly requires the nuclei mapping described in Eq. 5.8 to calculate the alchemical potential. We have calculated the barrier for the umbrella flipping of ammonia. NH_3 has two degenerate energy minima, a pyramidal structure with C_{3v} symmetry and its mirror plane conformer. Figure 5.2(A) shows a nudged elastic band [105, 106] calculation of the flipping barrier with a planar transition state and an activation energy of 0.21 eV.

We are interested in how the flipping barrier changes as we alchemically

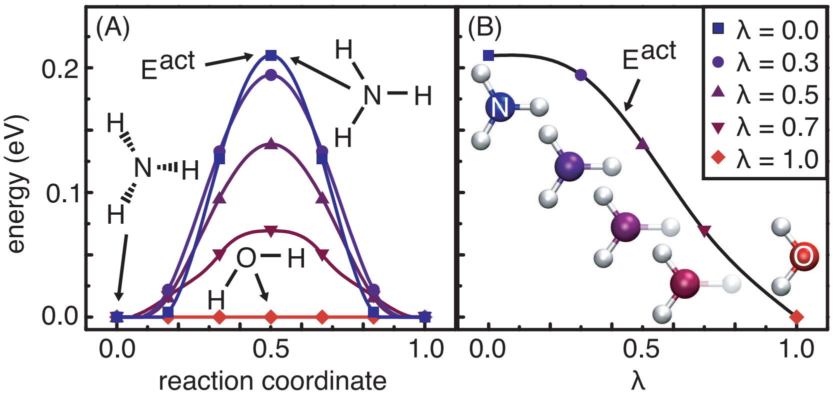

Figure 5.2: (A) The minimum energy path for the umbrella inversion of NH_3 passes through a planar transition state. This path is shown for several values of λ, where NH_3 ($\lambda = 0$) is alchemically transformed to H_2O ($\lambda = 1$). (B) E^{act} for the inversion process as a function of λ. The structures of the transition states are shown for select values of λ.

transform NH_3 into a different molecule – H_2O in this example. Water was chosen in part because it is a neighbor to ammonia in the alchemical space of molecules with unit changes in atomic numbers, and also because the flipping process for H_2O becomes a rotation with no energy barrier. This provides a convenient test case for the calculation of activation energies and the corresponding derivatives along an alchemical transformation where in the limit of $\lambda \to 1$, E^{act} is known *a priori* to be zero.

The alchemical transformation is defined by λ going from 0 to 1 as NH_3 is mutated to H_2O. We have chosen the transformation to correspond to the simultaneous addition of a proton the central atom and the annihilation of a H nucleus, linearly, as defined in Eq. (5.15). Figure 5.2(B) shows how the activation energy for the inversion barrier of NH_3 first decreases only slightly, then decays more rapidly, and finally vanishes as the molecule is transformed into H_2O.

The usefulness of alchemical derivatives for compound design can be measured by how well they can extrapolate to integer changes in N_I, corresponding to elements which exist in nature. For the alchemical transformation between NH_3 and H_2O, the $\{N_I\}$ change linearly in λ [Eq. (5.15)], but the property, E^{act} has significant curvature along λ. In Fig. 5.2(B), one can see how the linear extrapolation based on the derivative of E^{act} with respect to λ at H_2O would yield a reasonable prediction for the barrier of NH_3, whereas the derivative at NH_3 would significantly overestimate the flipping barrier at H_2O. Current efforts aim to determine alchemical paths that have first order derivatives that are more amenable to extrapolations to new compounds [85].

In previous work, relaxation of the force $\{\mathbf{F}_I\}$ for points along λ was only done for one structure because of the constraint, $\{\mathbf{R}_I^a\} = \{\mathbf{R}_I^b\}$ [107]. Using Eq. (5.8), this constraint is lifted, and the structures are relaxed independently. The most prominent geometry change of both the transition state and the initial state as ammonia is converted to water along λ, is the bond-length between the central atom and the hydrogen being annihilated. Figure 5.3 shows that the bond-length increases at the same rate for both the optimized initial state and the converged transition state. As the bond lengthens, the interaction between the fractional proton and the rest of the molecule decreases until it vanishes at $\lambda = 1$.

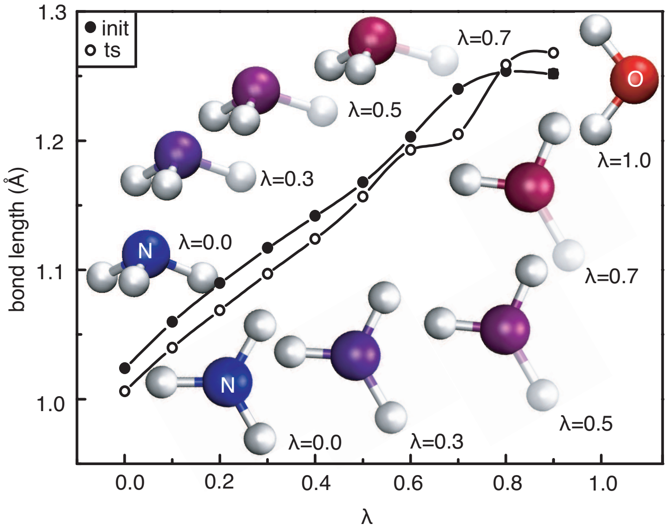

Figure 5.3: The bond distance between the central atom and the hydrogen being annihilated increases along λ for both the relaxed initial structure $\{\mathbf{R}_I^{\text{init}}\}$ and the relaxed transition state $\{\mathbf{R}_I^{\text{ts}}\}$ for the umbrella flipping process.

5.5.2 Protonation Energies

The second geometry-dependent property we discuss is the protonation energy for a set of iso-electronic molecules, CH_4, NH_3, H_2O, HF, and Ne. In the case of CH_4, for example, the protonation energy defined in Eq. (5.11) is $E^{\text{prot}} = E^{\text{CH}_4+\text{H}^+} - E^{\text{CH}_4} - E^{\text{H}^+}$. The choice of this property is motivated by the fact that it can be evaluated both for frozen and relaxed geometries, allowing to measure the effect of geometry relaxation when calculating alchemical derivatives.

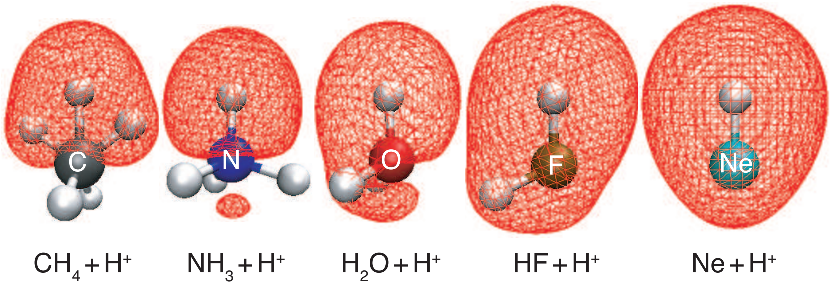

Figure 5.4: Isosurfaces of the alchemical potential $\mu_n^{\text{prot}}(\mathbf{r}) = 7$ eV from Eq. (5.12) are shown for the protonated methane series using geometries fixed to NH_4^+.

5.5.2.1 Fixed Geometries

In the case of fixed geometries we chose the relaxed NH_4^+ structure as the common structure for all of the molecules. For different molecules, such as H_2O, the central atom, O, was located at the N position and the two hydrogen atoms were in two of the four equivalent H positions. In the case of CH_5^+ an extra hydrogen atom was relaxed in the fixed NH_4^+ structure, and then kept fixed for its alchemical transformation.

With fixed geometries the alchemical potential for protonation is defined over all space according to Eq. (5.12). This is a useful function because it shows where a new atom should be added to change a desired property—in this case the protonation energy. Figure 5.4 shows isosurfaces of the alchemical potential $\mu_n^{\text{prot}}(\mathbf{r})$ for all the five compounds. Inside each of these surfaces, the change in energy is over 7 eV/proton for the molecule shown as compared to the de-protonated molecule without the uppermost proton. We note some features of the alchemical potential. First, the potential is very high around the uppermost proton because this is the proton which was added to calculate the protonation energy. Adding further proton density near this same location gives rise to the high electrostatic potential. Second, as one would expect from the Coulomb-explosion of water, the alchemical potential is always positive, indicating that at no point in space does the alchemical addition of an extra proton to the system favor the protonation energy–the energy of protonation increases as protons are added.

The alchemical change we have considered is an increase in the nuclear number of the central atom. At the same time, the proton in a bonded H atom is eliminated so the total number of protons is constant over the sequence of alchemical transformations, $CH_4 \rightarrow NH_3$, $NH_3 \rightarrow H_2O$, $H_2O \rightarrow HF$, and $HF \rightarrow Ne$. The alchemical potential of protonation is positive for each of these molecules, but the alchemical derivative along these paths also includes the proton annihilation. The change in protonation energy along these paths is the difference in alchemical potentials at the central atom and at the proton being removed. Figure 5.5 shows how the protonation energies change along the alchemical transformations, and how the difference in energy between the unfavorable addition of a proton at the center nucleus and the favorable H annihilation can lead to a lower overall energy. Fractional nuclei are treated using the numerical interpolations described in Sec. 5.3.5 so that energies can be calculated along the alchemical mutation.

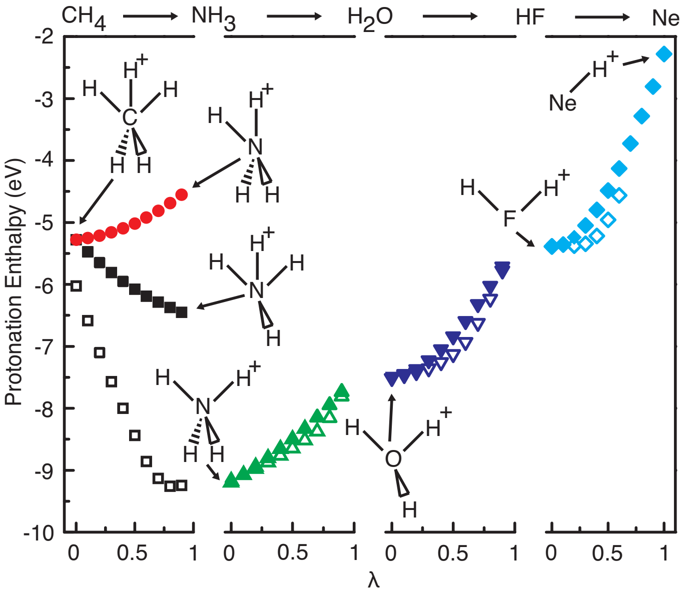

Figure 5.5: Left to right is the protonation energy as CH_4 is alchemically transformed into Ne. The structures shown as insets are the protonated endpoints whose pseudopotentials have been interpolated when following alchemical paths. For each alchemical path the number of protons on the central nucleus is increased by one and a hydrogen nucleus is concurrently annihilated. The solid symbols represent configurations fixed to the optimal NH_4^+ geometry and the empty symbols are relaxed. A consequence of using fixed structures is that all hydrogens are symmetrically equivalent for the CH_5^+ geometry; two separate paths emerge by selecting which hydrogen is to be annihilated.

5.5.2.2 Relaxed Geometries

The effect of molecular relaxation is shown in Fig. 5.5 to be particularly significant for the first transformation between CH_4 and NH_3. There are two possible alchemical transformations between these molecules in a fixed geometry case because the protonated CH_5^+ molecule has symmetrically nonequivalent protons, those which are neighboring the protonating H^+ and those which are not. The two different alchemical paths correspond to which type of proton is being annihilated. Upon relaxation, the asymmetry is removed as the molecules move to a single minimum energy structure. As one would expect, the difference between the fixed-geometry and relaxed-geometry paths are most significant for molecules which are highly strained, such as the NH_4^+ endpoint of the first transition. In the subsequent transitions, the fixed and relaxed geometries are much closer. As in the case of ammonia inversion, there is a significant curvature in the alchemical paths which reduces the predictive quality of the alchemical derivatives for integer changes in N_I.

5.5.3 Alchemical Potentials

To separate and validate the derivatives in Eq. (5.2) we focus only on the alchemical term, $\partial_\lambda E = \int d\mathbf{r}\, \mu_n(\mathbf{r})\, \partial_\lambda Z(\mathbf{r})$, as specified in Eq. (5.3). This is accomplished by choosing a system where N_e is constant, i.e. $\partial_\lambda N_e = 0$. The second term in Eq. (5.2) is also zeroed by relaxing the ions along the path so $\{\mathbf{F}_I\} = 0$. We have a particular interest in validating the analytical calculation of $\Delta\mu_{n,I}$ from Eq. (5.7) because it is from this calculation that

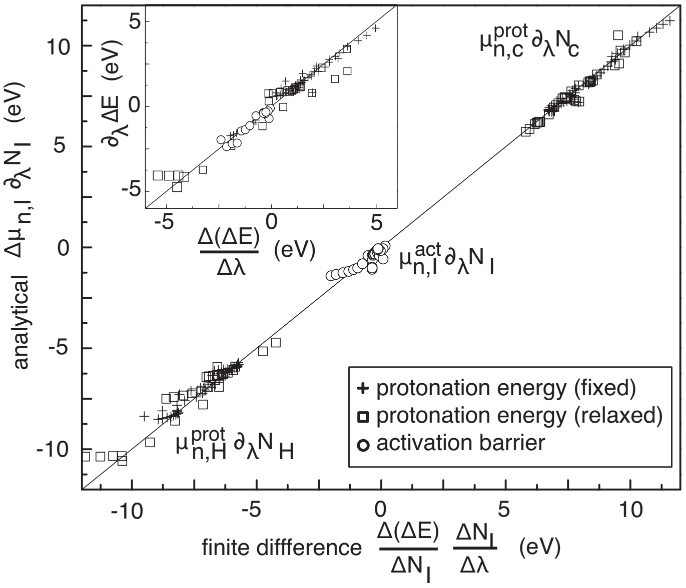

Figure 5.6: Correlation of the analytical [Eq. (5.9)] and numerical [Eq. (5.13)] alchemical derivatives $\Delta\mu_{n,\mathrm{H}}\,\partial_\lambda N_\mathrm{H}$ and $\Delta\mu_{n,\mathrm{c}}\,\partial_\lambda N_\mathrm{c}$, for all paths and all values of λ. The inset shows a similar correlation for the sum of these atomic components, which give derivatives of the binding and activation energies along the alchemical paths in Table 5.2.

$\partial_\lambda \Delta E$ depends, to first order.

In this study, every transforming path involves the alchemical mutation of two atoms, the simultaneous annihilation of a proton in a hydrogen atom and the increase of the atomic number of a central atom to which it is bound. As such, Eq. (5.9) is only non-zero for changes at the central atom and the annihilated hydrogen and reduces to $\partial_\lambda E = \Delta\mu_{n,\mathrm{H}}\,\partial_\lambda N_\mathrm{H} + \Delta\mu_{n,\mathrm{c}}\,\partial_\lambda N_\mathrm{c}$, where H and c indicate the hydrogen and central atom, respectively. For our linear transformations, $\partial_\lambda N_\mathrm{c} = -\partial_\lambda N_\mathrm{H} = 1$.

In Fig. 5.6 the accuracy of the individual terms $\Delta\mu_{n,\mathrm{H}}\,\partial_\lambda N_\mathrm{H}$ and $\Delta\mu_{n,\mathrm{c}}\,\partial_\lambda N_\mathrm{c}$ are compared separately to finite difference derivatives in λ as obtained from Eq. (5.13). The data is for all paths at each intermediate λ values considered for this study. For the two applications, barrier and reaction enthalpy, we have computed the alchemical potential terms according to Eqs. (5.10, 5.12). We find a correlation with a root-mean-square deviation of 0.29 eV for the barriers, and 0.26 eV (fixed-geometry) and 0.44 eV (relaxed-geometry) for the reaction enthalpies. The remaining deviation from the finite difference results is most likely due to the pseudopotential interpolation used to calculate $\frac{\Delta N_I}{\Delta\lambda}$ which is not the same as the analytical $\partial_\lambda Z$. Nonetheless, the pseudopotential is designed to model an atom with atomic number Z, so that linear changes in the pseudopotential are a reasonable approximation to linear changes in Z.

5.5.4 Oxygen Binding on a Pd Nanoparticle

For the alchemical potential to be useful for rational compound design it must be predictive for changes in the property of interest between real materials. Consequently, the potential must be sufficiently accurate in predicting changes to the property, and ideally the property should depend linearly on N_I. The numerical accuracy of the analytical alchemical potential has been demonstrated in the previous sections. Here, we address the predictive quality for the binding of molecular oxygen to the hollow site in the center of the (111) face of a 79 atom Pd nanoparticle. The property can be expressed in the form

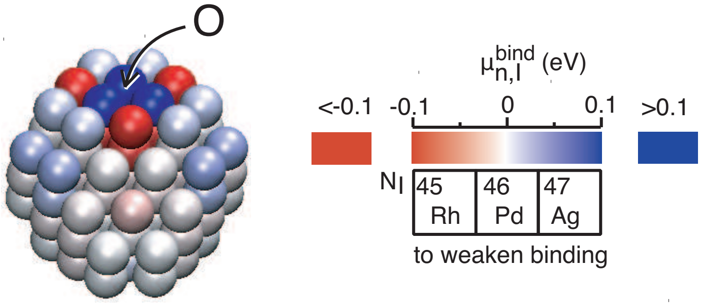

Figure 5.7: The alchemical potential $\mu^{\text{bind}}_{n,I}$, calculated from Eqs. (5.8,5.17), for the binding of O to a 79 atom Pd nanoparticle. Colors represent the value of the alchemical potential on each atom. To weaken oxygen binding atoms colored in red should be changed to the more noble Ag and atoms colored in blue should be changed to Rh. The opposite transformations should be made to strengthen the oxygen bond.

of Eq. (5.11) as

$$E^{\text{bind}} = E^{\text{Pd79+O}} - E^{\text{Pd79}} - \frac{1}{2}E^{\text{O}_2}. \tag{5.17}$$

As in the previous examples, we isolate the first, nuclear term of Eq. (5.2) by relaxing all geometries ($\{\mathbf{F}_I\} = 0$), and by performing exclusively iso-electronic changes ($\partial_\lambda N_e = 0$). We constrain all transitions to charge neutral paths by pairing the addition of a proton to any nucleus with the removal of a proton from a second nucleus in the system. Furthermore, we restrict ourselves to geometrically stable particles with D_{4h}-symmetry.

Figure 5.7 shows the alchemical potential for the binding energy of oxygen to the nanoparticle. The extreme values for $\mu^{\text{bind}}_{n,I}$ are on the (111) face where the O-atom binds; they fall off with distance from the binding site. If the goal is to tune the binding energy to a desired value, $\mu^{\text{bind}}_{n,I}$ can be

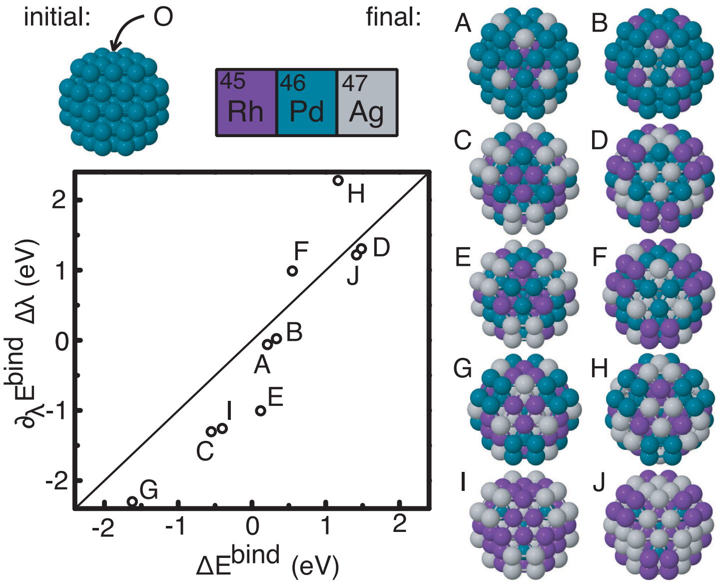

Figure 5.8: Correlation of alchemically predicted changes, $\partial_\lambda E^{\text{bind}}\Delta\lambda$ for $\Delta\lambda = 1$, with actual changes to the binding energy, ΔE^{bind}, of molecular oxygen to a 79 atom Pd cluster (initial) due to integer variations in atomic numbers (final).

used to decide which atoms in the system to alchemically change and in what direction. The best pure-metal for the oxygen reduction reaction is Pt, which binds O more weakly than Pd. To weaken the binding, Fig. 5.7 shows that the atoms directly at the binding site should be made more noble by increasing N_I. Alternatively, the second-neighbors can be made less noble by decreasing N_I, which is consistent with the ligand effect of near surface alloys [108, 109, 110].

Figure 5.8 shows the correlation between the actual change in calculated binding energy due to mutation, ΔE^{bind}, and the predicted change in binding energy, $\partial_\lambda E^{\text{bind}}\Delta\lambda$ for $\Delta\lambda = 1$, based on the sum over alchemical potentials in Eq. (5.9). Final structures A and B have 24, structures C-H have 48, and structures I-J have 72, nuclei alchemically changed from the initial 79 atom Pd particle, respectively. All actual changes have been obtained for geometrically relaxed complexes. The correlation between the prediction from the alchemical potential evaluated at the initial Pd particle and the calculated change in O binding for the alchemically modified final particles is very reasonable. Even for changes of up to 72 of the 79 atoms in the Pd particle, the alchemical potentials give a decent prediction for the change in the O binding energy. We emphasize that the computational cost for obtaining the predicted changes in binding energy correspond to a single evaluation of the binding energy for oxygen to the initial 79 atom Pd cluster.

5.6 Conclusions

We have presented numerical evidence that accurate analytical derivatives can be computed for chemical properties that involve variations in geometry. While test systems show some non-linearity in the alchemical paths, the derivatives can be predictive for integer changes in the number of protons as seen in the binding energy of oxygen to a Pd nanoparticle. Furthermore, once the the property of interest has been calculated for the initial compound, the corresponding alchemical derivative can be evaluated with negligible additional cost. Then, the effect of alchemical changes throughout the system can be estimated without doing additional calculations for all the various possible final compounds. This is a promising initial step towards the use of alchemical derivatives for the gradient-based optimization of materials.

5.6.1 Acknowledgments

This work was funded by the National Science Foundation (CHE-0645497), the Department of Energy under contract DE-FG02-09ER16090 and the Welch Foundation (F-1601). D. S. is grateful for support from the Sandia National Laboratory (SNL) summer student internship program at the Computer Science Research Institute. OAvL acknowledges support from SNL Truman Program Laboratory Directed Research Development project No. 120209. Sandia is a multiprogram laboratory operated by Sandia Corporation, a Lockheed Martin Company, for the United States Department of Energy's National Nuclear Security Administration under contract DE-AC04-94AL85000. We gratefully acknowledge the Texas Advanced Computing Center for computational resources.

Chapter 6

Application of Alchemical Derivatives for Catalyst Design

In Chapter 5 we showed that alchemical derivatives were predictive for the binding energy of molecular oxygen to a 79 atom Pd nanoparticle. In this chapter I look at the industrialy relevant problem of using alchemical derivatives to design a catalyst for the oxidation reduction reaction (ORR). The ORR reaction is the limiting reaction in fuel cell cathodes so optimizing a catalyst for this reaction is an important step toward fuel cell efficiency. Nørskov *et al.* showed that the binding energy of O to a metal surface is directly linked to the metal's catalytic activity[92]. We will use the binding of O to Pt(111) as a target binding energy ($E^{\text{target}} = 1.63$ eV) because the Pt(111) surface is known to be a good catalyst for the ORR reaction. We want to minimize an object function,

$$P = (E^{\text{bind}} - E^{\text{target}})^2 \tag{6.1}$$

to determine the fitness of the new catalyst where E^{bind} is the binding of O to the 111 face a generic 79 atom nanoparticle. Eq. 5.17 can be rewritten for the binding of molecular oxygen of a 79 atom nanoparticle,

$$E^{\text{bind}} = E^{\text{nano79+O}} - E^{\text{nano79}} - \frac{1}{2}E^{\text{O}_2}. \tag{6.2}$$

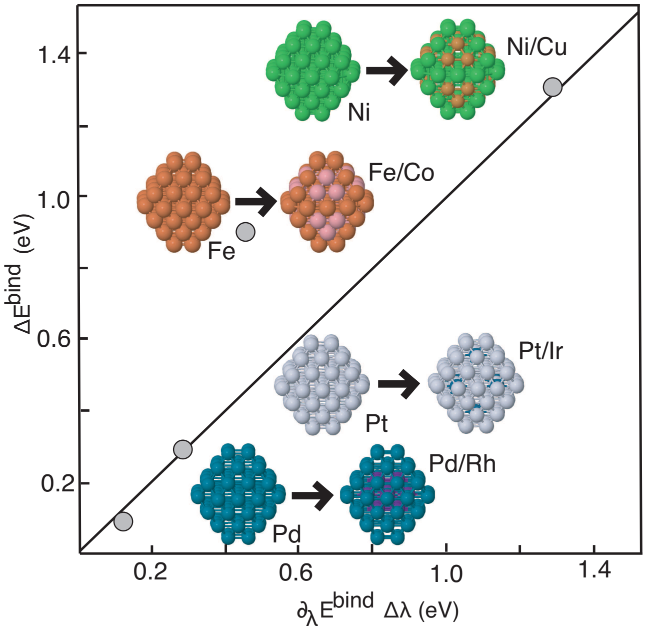

Figure 6.1: Alchemical derivatives from Eq. 6.3 are shown to be predictive for E^{bind}.

Calculations were performed using DFT as per Sec. 5.4 except using the PW91 form of the generalized gradient approximated exchange-correlation potential[28]. As in the Pd example, (5.5.4) all geometries are relaxed so $\{\mathbf{F}_I\} = 0$ in Eq. (5.2). However, we no longer constrain the system to iso-electronic changes ($\partial_\lambda N_e \neq 0$) so the electronic chemical potential (μ_e) term no longer disappears. Because we are using metal nanoparticles with delocalized valence electrons, μ_e is the fermi level and $\Delta\mu_e^{bind}$ is the change in the fermi level of the particle when oxygen binds to the surface. The resulting alchemical derivative for the O binding is

$$\partial_\lambda E^{\text{bind}} = \Delta\mu_e^{\text{bind}}\ \partial_\lambda N_e + \sum_I \Delta\mu_{n,I}^{\text{bind}}\ \partial_\lambda N_I. \tag{6.3}$$

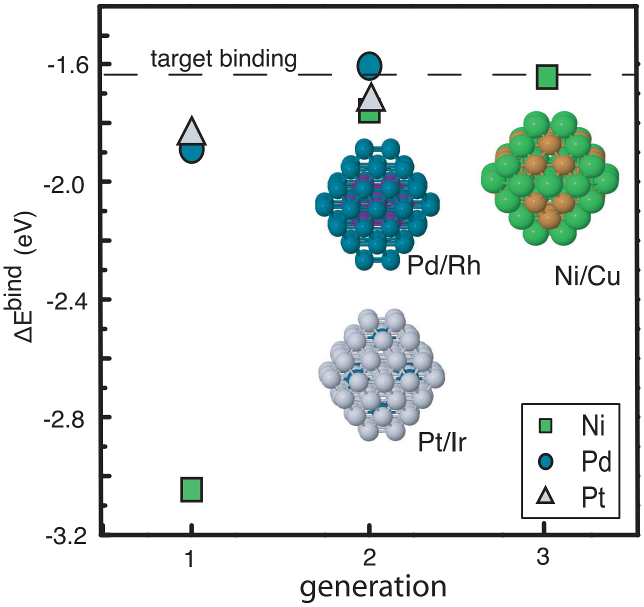

Figure 6.2: Three optimization steps using alchemical derivatives to tune E^{bind} to E^{target}.

Figure 6.1 shows that Eq. 6.3 is predictive for integer changes in N_I and changes N_e. The change due to μ_e is very small because the change in the fermi level of the particle upon O binding is small, ~0.002 eV/electron, it is however included for completeness. In Fig. 6.2 the first generation starts with pure Ni, Pd, and Pt nanoparticles. For convenience we restrict ourselves to geometrically stable particles with D_{4h}-symmetry which reduced the alchemical dimensionality to 14 atom types. Using a list of alchemical potentials from Eq. 6.1 we were visually able to determine a reasonable step to minimize Eq. 6.3. For a system with higher alchemical dimensionality, a discrete optimization algorithm would be needed to choose optimal alchemical mutations.

The Ni particle is optimized one more generation until E^{bind} is sufficiently close to E^{target}. The resulting catalyst candidates can now be suggested to experimentalist as a guide to synthesize a marketable catalyst for the ORR in fuel cells.

Bibliography

[1] G. H. Vineyard. Frequency factors and isotope effects in solid state rate processes. *J. Phys. Chem. Solids*, 3:121–127, 1957.

[2] J. K. Nørskov, T. Bligaard, J. Rossmeisl, and C. H. Christensen. Towards the computational design of solid satalysts. *Nature*, 121:37–46, 2009.

[3] H. Jónsson, G. Mills, and K. W. Jacobsen. Nudged elastic band method for finding minimum energy paths of transitions. In B. J. Berne, G. Ciccotti, and D. F. Coker, editors, *Classical and Quantum Dynamics in Condensed Phase Simulations*, pages 385–404. World Scientific, Singapore, 1998.

[4] G. Henkelman and H. Jónsson. Improved tangent estimate in the nudged elastic band method for finding minimum energy paths and saddle points. *J. Chem. Phys.*, 113:9978–9985, 2000.

[5] G. Henkelman, B. P. Uberuaga, and H. Jónsson. A climbing image nudged elastic band method for finding saddle points and minimum energy paths. *J. Chem. Phys.*, 113:9901–9904, 2000.

[6] S. A. Trygubenko and D. J. Wales. A doubly nudged elastic band method for finding transition states. *J. Chem. Phys.*, 120:2082–2094, 2004.

[7] W. E, W. Ren, and E. Vanden-Eijnden. String method for the study of rare events. *Phys. Rev. B*, 66:052301–1–4, 2002.

[8] W. E, W. Ren, and E. Vanden-Eijnden. Simplified and improved string method for computing the minimum energy paths in barrier-crossing events. *J. Chem. Phys.*, 126:164103–1–8, 2007.

[9] L. R. Pratt. A statistical method for identifying transition states in high dimensional problems. *J. Chem. Phys.*, 85:5045–5048, 1986.

[10] R. Elber and M. Karplus. A method for determining reaction paths in large molecules: Application to myoglobin. *Chem. Phys. Lett.*, 139:375, 1987.

[11] L. Xie, H. Liu, and W. Yang. Adapting the nudged elastic band method for determining minimum-energy paths of chemical reactions in enzymes. *J. Chem. Phys.*, 120:8039–8052, 2004.

[12] G. Henkelman and H. Jónsson. A dimer method for finding saddle points on high dimensional potential surfaces using only first derivatives. *J. Chem. Phys.*, 111:7010–7022, 1999.

[13] L. J. Munro and D. J. Wales. Defect migration in crystalline silicon. *Phys. Rev. B*, 59:3969, 1999.

[14] E. Bitzek, P. Koskinen, F. Fähler, M. Moseler, and P. Gumbsch. Structural relaxation made simple. *Phys. Rev. Lett.*, 97:170201–1–4, 2006.

[15] M. R. Hestenes and E. Steifel. Methods of conjugate gradients for solving linear systems. *J. Research Nat. Bur. Standards*, 49:409–436, 1952.

[16] W. H. Press, S. A. Teukolsky, W. T. Vetterling, and B. P. Flannery. *Numerical recipes in C: The art of scientific computation.* Cambridge University Press, Cambridge, 2nd edition, 1992.

[17] J. Nocedal. Updating quasi-Newton matrices with limited storage. *Mathematics of Computation*, 35:773–782, 1980.

[18] H. C. Andersen. Molecular dynamics simulations at constant pressure and/or temperature. *J. Chem. Phys.*, 72:2384–2393, 1980.

[19] D. J. Wales. *OPTIM: A program for optimizing geometries and calculating reaction pathways.* University of Cambridge Press, Cambridge, U.K., 2003. <http://www-wales.ch.cam.ac.uk/software.html>.

[20] J. M. Carr, S. A. Trygubenko, and D. J. Wales. Finding pathways between distant local minima. *J. Chem. Phys.*, 122:234903–1–7, 2005.

[21] G. Henkelman, G. Jóhannesson, and H. Jónsson. Methods for finding saddle points and minimum energy paths. In S.D. Schwartz, editor, *Progress on Theoretical Chemistry and Physics*, pages 269–299. Kluwer Academic, New York, 2000.

[22] D. W. Bassett and P. R. Webber. Diffusion of single adatoms of platinum, iridium and gold on platinum surfaces. *Surf. Sci.*, 70:520, 1978.

[23] P. Maragakis, S. A. Andreev, Y. Brumer, D. R. Reichman, and E. Kaxiras. Adaptive nudged elastic band approach for transition state calculation. *J. Chem. Phys.*, 117:4651–4658, 2002.

[24] J.-W. Chu, B. L. Trout, and B. R. Brooks. A super-linear minimization scheme for the nudged elastic band method. *J. Chem. Phys.*, 119:12708–12717, 2003.

[25] E. F. Koslover and D. J. Wales. Comparison of double-ended transition state search methods. *J. Chem. Phys.*, 127:134102, 2007.

[26] R. Malek and N. Mousseau. Dynamics of Lennard-Jones clusters: A characterization of the activation-relaxation technique. *Phys. Rev. E*, 62:7723–7728, 2000.

[27] L. Xu, G. Henkelman, C. T. Campbell, and H. Jónsson. Small Pd clusters, up to the tetramer at least, are highly mobile on the MgO(100) surface. *Phys. Rev. Lett.*, 95:146103–1–4, 2005.

[28] J. P. Perdew. Unified theory of exchange and correlation beyond the local density approximation. In P. Ziesche and H. Eschrig, editors, *Electronic Structure of Solids*, page 11. Akademie Verlag, Berlin, 1991.

[29] D. Vanderbilt. Soft self-consistent pseudopotentials in a generalized eigenvalue formalism. *Phys. Rev. B*, 41:7892–7895, 1990.

[30] G. Kresse and J. Joubert. From ultrasoft pseudopotentials to the projector augmented wave method. *Phys. Rev. B*, 59:1758, 1999.

[31] H. J. Monkhorst and J. D. Pack. Special points for Brillouin-zone integrations. *Phys. Rev. B*, 13:5188–5192, 1976.

[32] B. Peters, A. Heyden, A. T. Bell, and A. Chakraborty. A growing string method for determining transition states: Comparison to the nudged elastic band and string methods. *J. Chem. Phys.*, 120:7877–7886, 2004.

[33] G. A. Cisneros, H. Liu, Z. Lu, and W. Yang. Reaction path determination for quantum mechanical/molecular mechanical modeling of enzyme reactions by combining first order and second order "chain-of-replicas" methods. *J. Chem. Phys.*, 122:114502, 2005.

[34] S. K. Burger and W. Yang. Quadratic string method for determining the minimum-energy path based on multiobjective optimization. *J. Chem. Phys.*, 124:054109–1–13, 2006.

[35] See: <http://theory.cm.utexas.edu/henkelman/code>.

[36] D. Sheppard, R. Terrell, and G. Henkelman. Optimization methods for finding minimum energy paths. *J. Phys. Chem.*, 128:134106, 2008.

[37] W. Quapp and J. M. Bofill. A comment to the nudged elastic band method. *J. Comput. Chem.*, 31:2526–2531, 2010.

[38] M. Hirsch and W. Quapp. The reaction pathway of a potential energy surface as curve with induced tangent. *Chem. Phys. Lett.*, 395:150–156, 2004.

[39] A. Aguilar-Mogas, X. Giménez, and J. M. Bofill. Implementation of an algorithm based on the Runge-Kutta-Fehlberg technique and the potential energy as a reaction coordinate to locate intrinsic reaction paths. *J. Comput. Chem.*, 31:2510–2525, 2010.

[40] Y. Tiwary and K. A. Fichthorn. Mechanisms of atomic diffusion on the flat, stepped, and faceted surfaces of al(110). *Phys. Rev. B.*, 81:195421, 2010.

[41] S.-C. Li, Z. Zhang, D. Sheppard, B. D. Kay, J. M. White, Y. Du, I. Lyubinetsky, G. Henkelman, and Z. Dohnálek. Intrinsic diffusion of hydrogen on rutile $TiO_2(110)$. *J. Am. Chem. Soc.*, 130:9080, 2008.

[42] T. L. Thompson and J. T. Yates. TiO_2-based photocatalysis: Surface defects, oxygen and charge transfer. *Top. Catal*, 35:197, 2005.

[43] M. Grätzel. Photoelectrochemical cells. *Nature*, 414:338, 2001.

[44] A. Fujishima. Electrochemical photolysis of water at a semiconductor electrode. *Nature*, 238:37, 1972.

[45] A. L. Linsebigler, G. Q. Lu, and J. T. Yates. Photocatalysis on TiO_2 surfaces: Principles, mechanisms, and selected results. *Chem. Rev.*, 95:735, 1995.

[46] U. Diebold. The surface science of titanium dioxide. *Surf. Sci. Rep.*, 48:53, 2003.

[47] Z. R. Zhang, O. Bondarchuk, J. M. White, B. D. Kay, and Z. Dohnálek. Imaging adsorbate OH bond cleavage: Methanol on $TiO_2(110)$. *J. Am. Chem. Soc.*, 128:4198, 2006.

[48] M. A. Henderson. The interaction of water with solid surfaces: fundamental aspects revisited. *Surf. Sci. Rep.*, 46:5, 2002.

[49] M. A. Henderson, S. Otero-Tapia, and M. E. Castro. The chemistry of methanol on the $TiO_2(110)$ surface: the influence of vacancies and coadsorbed species. *Faraday Discuss.*, page 313, 1999.

[50] O. Bondarchuk, Y. K. Kim, J. M. White, J. Kim, B. D. Kay, and Z. Dohnálek. Surface chemistry of 2-propanol on $TiO_2(110)$: Low- and high-temperature dehydration, isotope effects, and influence of local surface structure. *J. Phys. Chem. C*, 111:11059, 2007.

[51] Z. Dohnálek, J. Kim, O. Bondarchuk, J. M. White, and B. D. Kay. Physisorption of N_2, O_2, and co on fully oxidized $TiO_2(110)$. *J. Phys. Chem. B*, 110:6229, 2006.

[52] S. Suzuki, K. Fukui, H. Onishi, and Y. Iwasawa. Hydrogen adatoms on TiO_2(110)-(1×1) characterized by scanning tunneling microscopy and electron stimulated desorption. *Phys. Rev. Lett.*, 84:2156, 2000.

[53] R. Schaub, R. Thostrup, N. Lopez, E. Laegsgaard, I. Stensgaard, J. K. Nørskov, and F. Besenbacher. Oxygen vacancies as active sites for water dissociation on rutile TiO_2(110). *Phys. Rev. Lett.*, 87:266104, 2001.

[54] O. Bikondoa, C. L. Pang, R. Ithnin, C. A. Muryn, H. Onishi, and G. Thornton. Direct visualization of defect-mediated dissociation of water on TiO_2(110). *Nat. Mater.*, 5:189, 2006.

[55] I. M. Barookes, C. A. Muryn, and G. Thornton. Imaging water dissociation on TiO_2(110). *Phys. Rev. Lett.*, 87:266103, 2001.

[56] M. A. Henderson. An HREELS and TPD study of water on TiO_2(110): the extent of molecular versus dissociative adsorption. *Surf. Sci.*, 355:151, 1996.

[57] M. A. Henderson, W. S. Epling, C. H. F. Peden, and C. L. Perkins. Insights into photoexcited electron scavenging processes on TiO_2 obtained from studies of the reaction of O_2 with OH groups adsorbed at electronic defects on TiO_2(110). *J. Phys. Chem. B*, 107:534, 2003.

[58] S. Wendt, R. Schaub, J. Matthiesen, E. K. Vestergaard, E. Wahlstrom, M. D. Rasmussen, P. Thostrup, L. M. Molina, E. Laegsgaard, I. Stensgaard, B. Hammer, and F. Besenbacher. Oxygen vacancies on TiO_2(110) and their interaction with H_2O and O_2: A combined high-resolution STM and DFT study. *Surf. Sci.*, 598:226, 2005.

[59] Z. R. Zhang, O. Bondarchuk, J. M. White, B. D. Kay, and Z. Dohnálek. Imaging water dissociation on TiO_2(110): Evidence for inequivalent geminate OH groups. *J. Phys. Chem. B*, 110:21840, 2006.

[60] Z. R. Zhang, Q. F. Ge, S.-C. Li, B. D. Kay, J. M. White, and Z. Dohnálek. Imaging intrinsic diffusion of bridge-bonded oxygen vacancies on TiO_2(110). *Phys. Rev. Lett.*, 99:126105, 2007.

[61] S. Wendt, J. Matthiesen, R. Schaub, E. K. Vestergaard, E. Laegsgaard andnd F. Besenbacher, and B. Hammer. Formation and splitting of paired hydroxyl groups on reduced TiO_2(110). *Phys. Rev. Lett.*, 96:066107, 2006.

[62] G. Kresse and J. Hafner. Ab initio molecular-dynamics simulation of the liquid-metal amorphous-semiconductor transition in germanium. *Phys. Rev. B*, 49:14251–14269, 1994.

[63] V. Cristiana Di, P. Gianfranco, and S. Annabella. Electronic structure of defect states in hydroxylated and reduced rutile TiO_2(110) surfaces. *Phys. Rev. Lett.*, 97:166803, 2006.

[64] J. D Wrigley, M. E. Twigg, and G. Ehrlich. Lattice walks by long jumps. *J. Chem. Phys.*, 93:2885, 1990.

[65] S. Kajita, T. Minato, H. S. Kato, M. Kawai, and T. Nakayama. First-principles calculations of hydrogen diffusion on rutile TiO_2(110) surfaces. *J. Chem. Phys.*, page 127, 2007.

[66] E. Wigner. The transition state method. *Trans. Faraday Soc.*, 34:0029, 1938.

[67] G. Henkelman, A. Arnaldsson, and H. Jónsson. Theoretical calculations of CH_4 and H_2 associative desorption from Ni(111): Could subsurface hydrogen play an important role? *J. Chem. Phys.*, 124:044706, 2006.

[68] H. S. Johnston. *Gas Phase Reaction Theory.* The Ronald Press Co., Ronald NY, 1966.

[69] R. L. Kurtz, R. Stock-Bauer, T. E. Madey, E. Roman, and J. De Segovia. Synchrotron radiation studies of H_2O adsorption on TiO_2(110). *Surf. Sci.*, 218:178, 1998.

[70] S. Krischok, O. Hofft, J. Gunster, J. Stultz, D. W. Goodman, and V. Kempter. H_2O interaction with bare and Li-precovered TiO_2: studies with electron spectroscopies (MIES and UPS(Hei and ii)). *Surf. Sci.*, 495:8, 2001.

[71] B. J Morgan and G. W. Watson. A DFT + U description of oxygen vacancies at the TiO_2 rutile (110) surface. *Surf. Sci.*, 601:5034, 2007.

[72] R. F. W. Bader. *Atoms in Molecules: A Quantum Theory.* Oxford Univ. Press, USA, 1990.

[73] G. Henkelman, A. Arnaldsson, and H. Jónsson. A fast and robust algorithm for bader decomposition of charge density. *Comp. Mat. Sci.*, 36:354, 2006.

[74] L. C. Blum and J.-L. Reymond. 970 million druglike small molecules for virtual screening in the chemical universe database gdb-13. *J. Am. Chem. Soc.*, 131:8732, 2009.

[75] T. Fink and J.-L. Reymond. Virtual exploration of the chemical universe up to 11 atoms of c, n, o, f: Assembly of 26.4 million structures (110.9 million stereoisomers) and analysis for new ring systems, stereochemistry, physicochemical properties, compound classes, and drug discovery. *J. Chem. Inf. Model.*, 47:342, 2007.

[76] B. K. Shoichet. A simple but reliable method for the prediction of intermolecular potentials. *Nature*, 432:862, 2004.

[77] R. Guha, D. Dutta, P. Jurs, and T. Chen. Local lazy regression: Making use of the neighborhood in improve qsar predictions. *jcim*, 46:1836, 2006.

[78] S. Zhang, A. Golbraikh, S. Oloff, H. Kohn, and A. Tropsha. A novel automated lazt learning qsar (all-qsar) approach: Method development, applications, and virtual screening of chemical databases using validated all-qsar models. *J. Chem. Inf. Model.*, 46:1984, 2006.

[79] A. Franceschetti and A. Zunger. The inverse band-structure problem of finding an atomic configuration with given electronic properties. *Nature*, 402:60, 1999.

[80] G. H. Jòhannesson, T. Bligaard, A. V. Ruban, H. L. Skriver, K. W. Jacobsen, and J. K. Nørskov. Combined electronic structure and evolutionary search approach to materials design. *Phys. Rev. Lett.*, 88:255506, 2002.

[81] T. Mueller and G. Ceder. Bayesian approach to cluster expansions. *Phys. Rev. B*, 80:024103, 2009.

[82] O. A. von Lilienfeld, R. Lins, and U. Rothlisberger. Variational particle number approach for rational compound design. *Phys. Rev. Lett.*, 95:153002, 2005.

[83] O. A. von Lilienfeld and M. E. Tuckerman. Molecular grand-canonical ensemble density functional theory and exploration of chemical space. *J. Chem. Phys.*, 125:154104, 2006.

[84] V. Marcon, O. A. von Lilienfeld, and D. Andrienko. Tuning electronic eigenvalues of benzene via doping. *J. Chem. Phys.*, 127:064305, 2007.

[85] O. Anatole von Lilienfeld. Accurate ab initio energy gradients in chemical compound space. *J. Chem. Phys.*, 131:164102, 2009.

[86] M. Wang, X. Hu, D. N. Beratan, and W. Yang. Designing molecules by optimizing potentials. *J. Am. Chem. Soc.*, 128:3228, 2006.

[87] D. Xiao, W. Yang, and D. N. Beratan. Inverse molecular design in a tight-binding framework. *J. Chem. Phys.*, 129:044106, 2008.

[88] X. Hu, D. N. Beratan, and W. Yang. A gradient-directed Monte Carlo approach to molecular design. *J. Chem. Phys.*, 129:064102, 2008.

[89] D. Balamurugan, W. Yang, and D. N. Beratan. Exploring chemical space with discrete, gradient, and hybrid optimization methods. *J. Chem. Phys.*, 129:174105, 2008.

[90] S. Keinan, M. J. Therien, D. N. Beratan, and W. Yang. Molecular design of porphyrin-based nonlinear optical materials. *J. Phys. Chem. A*, 112:12203, 2008.

[91] B. C. Rinderspacher, J. Andzelm, A. Rawlett, J. Dougherty, D. N. Beratan, and W. Yang. Discrete optimization of electronic hyperpolarizabilities in a chemical subspace. *J. Chem. Theory Comput.*, 5:3321–3329, 2009.

[92] J. K. Nørskov, J. Rossmeisl, A. Logadottir, L. Lindqvist, J. R. Kitchin, T. Bligaard, and H. Jónsson. Origin of the overpotential for oxygen reduction at a fuel-cell cathode. *J. Phys. Chem. B*, 108:17886–17892, 2004.

[93] J. G. Kirkwood. Statistical mechanics of fluid mixtures. *J. Chem. Phys.*, 3:300, 1935.

[94] R. W. Zwanzig. Hightemperature equation of state by a perturbation method. i. nonpolar gases. *J. Chem. Phys.*, 22:1420–1426, 1954.

[95] W. F. van Gunsteren, X. Daurab, and A. E. Markc. Computation of free energy. *Helv. Chim. Acta*, 85:3113, 2002.

[96] P. Hohenberg and W. Kohn. Inhomogeneous electron gas. *Phys. Rev.*, 136:B864, 1964.

[97] J. F. Janak. Proof that $\partial \mathrm{E}/\partial n_i = \epsilon_i$ in density-functional theory. *Phys. Rev. B*, 18:7165, 1978.

[98] P. Mori-Sánchez, A. J. Cohen, and W. Yang. Discontinuous nature of the exchange-correlation functional in strongly correlated systems. *Phys. Rev. Lett.*, 102:066403, 2009.

[99] W. Kohn and L. J. Sham. Self-consistent equations including exchange and correlation effects. *Phys. Rev.*, 140:A1133, 1965.

[100] J. P. Perdew, K. Burke, and M. Ernzerhof. Generalized gradient approximation made simple. *Phys. Rev. Lett.*, 77:3865, 1996.

[101] G. Kresse and J. Hafner. Ab initio molecular dynamics for liquid metals. *Phys. Rev. B*, 47:558, 1993.

[102] G. Kresse and J. Furthmller. Efficient iterative schemes for ab initio total-energy calculations using a plane-wave basis set. *Phys. Rev. B*, 54:11169, 1996.

[103] P. E. Blöchl. Projector augmented-wave method. *Phys. Rev. B*, 50:17953, 1994.

[104] G. Kresse and D. Joubert. From ultrasoft pseudopotentials to the projector augmented-wave method. *Phys. Rev. B*, 59:1758, 1999.

[105] G. Henkelman, B. P. Uberuaga, and H. Jónsson. A climbing imgage nudged elastic band method for finding saddle points and minimum energy paths. *J. Chem. Phys.*, 113:9901, 2000.

[106] D. Sheppard, R. Terrell, and G. Henkelman. Optimization methods for finding minimum energy paths. *J. Chem. Phys.*, 128:123106, 2008.

[107] O. A. von Lilienfeld and M. E. Tuckerman. Alchemical variation of intermolecular energies according to molecular grand-canonical ensemble density functional theory. *J. Chem. Theory Comput.*, 3:1083, 2007.

[108] J. Greeley, J. K. Nørskov, and M. Mavrikakis. Electronic structure and catalysis on metal surfaces. *Annu. Rev. Phys. Chem.*, 53:319, 2002.

[109] J. Zhang, M. B. Vukmirovic, K. Sasaki, A. U.Nilekar, M. Mavrikakis, and R. R. Adzic. Mixed-metal Pt monolayer electrocatalysts for enhanced oxygen reduction kinetics. *J. Am. Chem. Soc.*, 127:12480–12481, 2005.

[110] W. Tang and G. Henkelman. Charge redistribution in core-shell nanoparticles to promote oxygen reduction. *J. Chem. Phys.*, 130:194505, 2009.

Vita

Daniel Glen Sheppard was born in Los Alamos, New Mexico on the 26th of October 1982, the son of Dr. Maurice G. Sheppard and Jensina S. Sheppard. He then married his high school sweetheart, Julia R. Sorenson, in 2003 before receiving a Bachelor of Science degree in Chemistry from the University of California at Davis in 2005. He was accepted to the University of Texas at Austin for enrollment in their chemistry program and started his graduate studies in August, 2005. Upon completion of his Ph.D, he will be the third generation to achieve this level of education. While at the University, he served as captain and tournament chair for the University of Texas Graduate Rugby Club. To date, he has fathered six children who he expects to also pursue advanced degrees in the natural sciences.

Permanent address: 3350E Lake Austin Blvd.
Austin, Texas 78703

This dissertation was typeset with LaTeX[†] by the author.

[†] LaTeX is a document preparation system developed by Leslie Lamport as a special version of Donald Knuth's TeX Program.